

30 circulation in all three monsoon regions distributes PAN into the tropical latitude belt in the
31 upper troposphere (UT). Remote transport also occurs in the extratropical UT where westerly
32 winds drive North American and European pollutants eastward where they can become part of
33 the ASM convection and lifted into the lower stratosphere. In the lower stratosphere the injected
34 pollutants are transported westward by easterly winds. Sensitivity experiments with ECHAM5-
35 HAMMOZ for simultaneous NO_x and NMVOCs emission change (-10 %) over ASM, NAM,
36 WAM confirm similar transport. Our analysis shows that 10% change in Asian emissions,
37 transport ~5-30 ppt of PAN in the UTLS over Asia, ~1-10 ppt of PAN in the UTLS of Northern
38 subtropics and mid latitudes, ~7-10 ppt of HNO_3 and ~1-2 ppb of ozone in UT over Asia.
39 Comparison of emission change over Asia, North America and Africa shows highest transport of
40 HNO_3 and ozone occurs in the UT over Asia and least over Africa.

41 The intense convective activity in the monsoon regions is associated with lightning and
42 thereby the formation of additional NO_x . This also affects the distribution of PAN in the UTLS.
43 Simulations with and without lightning show an increase in the concentrations of PAN (~40 %),
44 HNO_3 (75%), NO_x (70 %) and ozone (30 %) over the regions of convective transport. Lightning
45 induced production of these species is higher over equatorial Africa and America as compared to
46 the ASM region. This indicates that the contribution of anthropogenic emission to PAN in the
47 UTLS over the ASM, is higher than that of lightning.

48

49

50

51 1. Introduction

52 Deep monsoon convection plays a key role in venting chemical constituents from the
53 boundary layer and their export from source regions (Dickerson et al., 1987). The largest
54 regional monsoon systems are the North American monsoon (NAM), Asian Summer Monsoon
55 (ASM), Western North Pacific monsoon (WNPM), South American monsoon (SAM), West
56 African Monsoon (WAM), and the Australian Monsoon (AUSM) (Chang et al., 2011). Recent
57 observation and modeling studies indicate that the Asian summer monsoon (Park et al., 2004; Li
58 et al., 2005; Randel and Park, 2006; Fu et al., 2006; Park et al., 2007; Xiong et al., 2009; Randel
59 et al., 2010; Fadnavis et al., 2013), the North American Monsoon (Schmitz and Mullen 1996;
60 Collier and Zhang, 2006; Barth et al., 2012) and the West African monsoon (Bouarar et al.,
61 2011) play important roles in the transport of chemical constituents out of the boundary layer
62 into the northern hemisphere in the Upper Troposphere (UT). A Number of studies have
63 documented that large amounts of pollution from Asia are transported across the tropopause
64 (Park, 2006; Fu et al., 2006; Park et al., 2007). However transport from other monsoon systems
65 (WAM, NAM) and their contribution to Asia have so far got less attention. Until now there has
66 been no attempt to assess the relative contributions from these source regions and to analyze the
67 transport patterns including possible recirculation within one consistent model framework. Prior
68 model simulations suggest that pollutants transported from the Asian monsoon region can
69 contribute substantially to the budgets of stratospheric ozone, NO_x and water vapour (Randel et
70 al., 2010). Ozone formation in the anticyclone is also enhanced by transport of pollution plumes
71 from the North American monsoon which are rich in volatile organic compounds (VOC) (Li et
72 al., 2005; Zhang et al., 2008; Choi et al., 2009; Barth et al., 2012). The deep monsoon convection
73 over West Africa transports Central African emissions to the upper troposphere and lower

74 stratosphere (UTLS) leading to large ozone changes in the lower stratosphere (Bouarar et al.,
75 2011). A number of studies have reported transport of chemical constituents into the UTLS due
76 to the Asian monsoon convection, while less attention has been paid to deep convective transport
77 from North/South America and West Africa to the lower stratosphere and to their relative
78 contributions to the UTLS composition over the ASM region.

79 This study investigates the transport patterns and relative contributions to the Asian monsoon
80 anticyclone of three oxidized nitrogen species, namely peroxyacetyl nitrate (PAN), NO_x (the sum
81 of NO and NO_2), and nitric acid (HNO_3). PAN is a secondary pollutant that marks the transport
82 and conversion of surface NO_x after it is emitted. The focus of this study is placed on PAN as
83 this species has a long lifetime (90-180 days) in the UT and can be favorably observed by
84 satellite instruments. At the same time its short chemical lifetime in the lower troposphere (not
85 longer than 30 days) results in a much tighter association between the emissions regions of its
86 precursors and transport compared to species such as carbon monoxide (CO). The much longer
87 chemical lifetime of CO in the lower troposphere allows it to reach the UTLS via circuitous
88 pathways that are not accessible to PAN. In contrast, PAN is a tracer that allows for a clearer
89 identification of NO_x pollution transport pathways between the surface and the UTLS. We
90 perform NO_x and MNVOCs emission sensitivity simulations (where emissions of NO_x and
91 MNVOCs were simultaneously reduced by 10%) in order to investigate the relative
92 contributions from Asia, Africa and America to the PAN, HNO_3 and O_3 concentrations in the
93 UTLS.

94 PAN is formed through oxidation of non methane volatile organic compounds (NMVOCs) in
95 the presence of NO_x (Fischer et al., 2014). It is primarily formed after oxidation of acetaldehyde
96 (CH_3CHO) or after photolysis of acetone (CH_3COCH_3) and methyl glyoxal (CH_3COCHO), all of

107 which are oxidation products of various NMVOCs. The actual formation of PAN proceeds in the
108 reaction of the peroxy acetyl radical (CH_3CO_3) with NO_2 . This reaction is reversible and the
109 thermal decomposition of PAN back to CH_3CO_3 and NO_2 is the main sink of PAN, although in
110 the UTLS PAN photolysis becomes the dominant loss process. Two minor loss processes of
111 PAN are reaction with OH and dry deposition (Talukdar et al., 1995; Fischer et al., 2014). As
112 stated by Fischer et al. (2014) globally, biogenic VOC like isoprene and terpenes contribute most
113 to PAN formation, but in the context of our study it is important to note that the oxidation of
114 many alkanes and alkenes which are emitted from anthropogenic sources lead to PAN formation
115 as well. The major anthropogenic sources of NMVOCs are the emissions from fossil fuel and
116 biofuel combustion and from industrial solvents (Tang et al., 2009). Biomass burning, biogenic
117 and soil emissions also contribute to NMVOC and NO_x production. Anthropogenic sources are
118 dominant in the extra tropical Northern Hemisphere outside the spring season. In spring, when
119 surface PAN peaks, biogenic and anthropogenic NMVOCs species are responsible for ~50% of
120 the PAN burden.

121 In the UT, lightning can add substantial amounts of NO_x and thus lead to additional PAN
122 production if NMVOC precursors are present, e.g. from convective uplifting from the boundary
123 layer (Tie et al., 2001). The estimated global NO_x production by lightning is ~3 - 5 Tg N/year
124 (Schumann and Huntrieser, 2007; Martin et al., 2007; Murray et al., 2012). Strong lightning
125 activity during ASM, NAM and WAM (Shepon, et al., 2007; Evett et al., 2008; Ranalkar and
126 Chaudhari, 2009; Barret et al., 2010; Penki and Kamra, 2013) hence contributes to PAN
127 production in the UTLS. The estimated increase in PAN is ~20 - 30 % due to NO_x enhancement
128 by lightning (Tie et al., 2001).

119 The thermal decomposition rate of PAN is highly temperature dependent. In the UTLS
120 temperatures are sufficiently low to prevent thermal decomposition of PAN and therefore the
121 chemical lifetime of PAN in this region is ~90 - 180 days (Arnold and Hauck, 1984). The PAN
122 lifetime in our ECHAM5-HAMMOZ simulations varies between 80 days and 170 days in the
123 tropical UTLS. Several studies (Tereszchuk et al., 2013, Glatthor et al., 2007, Sign et al 1987)
124 have reported that the lifetime of PAN varies between 2 - 4 months. PAN thus travels over long
125 distances and affects the NO_y partitioning in areas that are far away from the precursor emission
126 regions. Upon descent into warmer regions of the troposphere, PAN releases NO_x which in turn
127 increases ozone and OH production in remote regions (Singh et al., 1986; Singh et al., 1998;
128 Hudman et al., 2004). PAN mixing ratios vary from less than 1 pptv in the remote marine
129 atmosphere (as observed during the NASA GTE PEM-Tropics B campaign in the South Pacific
130 lower marine boundary layer, data available at <http://acd.ucar.edu/~emmons/DATACOMP/>) to
131 several ppbv in the polluted urban environment and biomass burning plumes (Ridley et al., 1992;
132 Singh et al., 1998). In the UTLS mixing ratios are typically in the range 10-300 pptv (Emmons et
133 al., 2000; Keim et al., 2008).

134 To our knowledge our study is the first study that analyzes the influence of monsoon outflow
135 from different world regions on the distribution of peroxyacetyl nitrate (PAN) in the UTLS over
136 the Asian monsoon region, and its recirculation in the UTLS. We run decadal simulations with
137 the chemistry climate model ECHAM5-HAMMOZ. In emission sensitivity experiments, NO_x
138 and NMVOCs emissions were simultaneously reduced by 10% over ASM, WAM and NAM to
139 understand regional contribution. We apply statistical comparisons with satellite and aircraft
140 data, thereby contributing to the objectives of the Chemistry Climate Model Initiative (CCMI,
141 see <http://www.igacproject.org/CCMI>). The model climatology is evaluated with data from

142 aircraft campaigns and the Michelson Interferometer for Passive Atmospheric Sounding
143 (MIPAS) instrument onboard the ENVironmental SATellite (ENVISAT) (Refereed as MIPAS-E
144 hereafter). The transport of HNO₃ and NO_x due to monsoon convection from different monsoon
145 regions and the impacts of lightning on the UTLS distributions of the nitrogen oxides are also
146 analyzed and compared to the results obtained for PAN. The paper is organized as follows:
147 Section 2 contains a short description of the data and model including the simulation setup.
148 Comparisons of model simulations with observations are given in section 3. In section 4, we
149 discuss the various convective transport pathways of PAN into the UTLS, its redistribution in the
150 stratosphere and its re-circulation across the various monsoon regions as well as results of the
151 emission sensitivity simulations depicting contribution from major monsoon systems. The
152 analysis of percentage changes in lightning produced ozone, HNO₃, PAN and NO_x on total
153 concentrations over the convective zones is presented in section 5. Conclusions are given in
154 section 6.

155

156 2. Methods

157 2.1 Satellite measurements

158 MIPAS-E instrument onboard the ENVISAT was launched in March 2002 into a polar orbit
159 of 800 km altitude, with an orbital period of about 100 minutes and an orbit repeat cycle of 35
160 days. MIPAS-E (Fischer and Oelhaf, 1996; Fischer et al., 2008) was a Fourier Transform
161 Spectrometer that provided continual limb emission measurements in the mid infrared over the
162 range $685 - 2410 \text{ cm}^{-1}$ ($14.6 - 4.15 \text{ }\mu\text{m}$). From January 2005 through the end of the mission in
163 April 2012 MIPAS was operated with a spectral resolution of 0.0875 cm^{-1} , and a stepping of the
164 tangent altitude of $1.5 - 2 \text{ km}$ in the UTLS region. As mid infrared sounder MIPAS-E could not
165 provide spectral information from below cloud top.

166 MIPAS-E monitored several atmospheric trace constituents affecting atmospheric chemistry
167 including PAN, NO_x , and O_3 . The details of the general retrieval method and setup, error
168 estimates and use of averaging kernel and visibility flag are documented by Von Clarmann et al.
169 (2009). In this study we analyze the MIPAS-E observed PAN data during the period 2005 –
170 2012, i.e. the data version V5R_PAN_220/V5R_PAN_221 (different naming 220/221 merely
171 due to technical reasons). The data are available from [http://share.lsd.fkit.edu/imk/asf/sat/mipas-](http://share.lsd.fkit.edu/imk/asf/sat/mipas-export/Data_by_Target/)
172 [export/Data_by_Target/](http://share.lsd.fkit.edu/imk/asf/sat/mipas-export/Data_by_Target/). Details of the MIPAS PAN retrievals, error budget, and vertical
173 resolution are given by Glatthor et al. (2007) and by Wiesele et al. (2012). Table 3 in Wiesele et
174 al. (2012) indicates that for the total error of single profiles of the V5R_PAN_220/221 product
175 the spectral noise and the uncertainty of the instrument pointing are the main contributors.
176 However, since noise is a major contributor a reduction of the total error can be expected for
177 vertical profiles of binned data. For typical bins used in this work the total errors are less than 10
178 % below 12 km, 30 % at 15 km, 50 % at 19 km and 80 % at 23 km.

179 The sensitivity of the PAN retrievals can be judged by the averaging kernels. For the
180 V5R_PAN_220/221 product an example of the respective averaging kernel rows is shown in
181 figure S1 for an altitude range of 5 to 25 km at 28 degree N and 85 degree E for cloud free
182 atmospheric conditions. The diamonds indicate the respective nominal altitudes of the retrieval
183 grid. The figure shows that the retrieval results below 8 - 9 km are dominated by information
184 from above the nominal altitude. A similar, albeit less obvious, situation develops for altitudes
185 above 22 - 23 km. There and above the information has an increasing weight from lower than
186 nominal altitudes. This is the reason why the MIPAS PAN data is not considered below 8 km
187 and above 23 km. Another effect clearly visible in the example is that the altitude region which
188 influences the retrieved PAN value at a given altitude is increasing with altitude, i.e. the vertical
189 resolution decreases with altitude. To account for the comparatively low, and altitude dependent,
190 vertical resolution, the model data to be directly compared to MIPAS measurements was
191 convolved with the MIPAS PAN averaging kernel.

192 The data are contoured and gridded at 4 degree latitude and 8 degree longitude resolution. In
193 the process the data quality specifications as documented at
194 <http://share.lsd.fkit.edu/imk/asf/sat/mipas-export/Documentation/> were employed, namely: only
195 data with visibility flag equal 1 and diagonal value of averaging kernel greater than 0.03 were
196 used.

197 **2.2 ECHAM5-HAMMOZ model simulation and experimental setup**

198 The ECHAM5-HAMMOZ aerosol-chemistry-climate model used in the present study
199 comprises of the general circulation model ECHAM5 (Roeckner et al., 2003), the tropospheric
200 chemistry module, MOZ (Horowitz et al., 2003), and the aerosol module, Hamburg Aerosol
201 Model (HAM) (Stier et al., 2005). It includes ozone, NO_x, VOC and aerosol chemistry. The gas

202 phase chemistry scheme is based on the MOZART-2 model (Horowitz et al., 2003), which
203 includes comprehensive O_x - NO_x -hydrocarbons chemistry with 63 tracers and 168 reactions. The
204 $O(^1D)$ quenching reaction rates were updated according to Sander et al. (2003), and isoprene
205 nitrates chemistry according to Fiore et al. (2005). In the model simulations we included
206 emissions of acetone from anthropogenic sources and wild fires (primary sources), while
207 acetaldehyde and methylglyoxal are produced by oxidation of other NMVOCs (secondary
208 sources). In particular, oxidation of primary NMVOCs like ethane (C_2H_6), propane (C_3H_8) and
209 propene (C_3H_6) forms acetaldehyde, while CH_3COCHO is mainly formed from the oxidation
210 products of isoprene and terpenes. Higher acyl peroxy nitrates (MPAN) have been included in
211 the MOZART-2 chemical scheme, which are also formed through oxidation of NMVOCs, but
212 their production is small compared to PAN. Thermal decomposition, and reaction with OH as
213 well as the absorption cross sections for PAN photolysis are all specified according to Sander et
214 al. (2003).

215 In ECHAM5-HAMMOZ dry deposition follows the scheme of Ganzeveld and Lelieveld
216 (1995). Soluble trace gases such as HNO_3 and SO_2 are also subject to wet deposition. In-cloud
217 and below cloud scavenging follows the scheme described by Stier et al. (2005). PAN is not
218 water soluble, therefore dry and wet deposition are insignificant removal processes.

219 The model is run at a spectral resolution of T42 corresponding to about 2.8×2.8 degrees in
220 the horizontal dimension and 31 vertical hybrid σ -p levels from the surface up to 10 hPa. We
221 note that the nominal grid resolution of 2.8 degrees is somewhat misleading, because the spectral
222 truncation of T42 only allows to resolve details on the order of $180/42 = 4.28$ degrees. This is the
223 main reason why we compare our model results with the MIPAS PAN retrievals on a 4×8

224 degree grid. The details of model parameterizations, emissions and validation are described by
225 Pozzoli et al., (2008a,b, 2011) and Fadnavis et al. (2013).

226 The model simulations were performed with varying monthly mean sea surface
227 temperature (SST) and sea ice cover (SIC) data over the period 2000 – 2010 (AMIP) referred as
228 control simulation. The simulations did not aim to exactly reproduce specific meteorological
229 years, and we ran 11-year periods in order to obtain a reasonable statistics. We used the RETRO
230 project data set of the year 2000 available at <http://eccad.sedoo.fr/> for the surface CO, NO_x, and
231 hydrocarbon emissions from anthropogenic sources and biomass burning (Schultz et al., 2004;
232 2005; 2007; 2008). Anthropogenic total RETRO emissions of the year 2000 are 476 Tg/year for
233 CO and 90 Tg/year for NO_x, 5 Tg/year of ethane, 3.5 Tg/year of propane and 2.7 Tg/year of
234 propene, which are the main anthropogenic VOC precursors of PAN. Biomass burning RETRO
235 emissions of year 2000 are 357 Tg/year for CO, and 16 Tg/year for NO_x. 2.5 Tg/year for ethane,
236 1.3 Tg/year for propane, 2.7 Tg/year for propene, and 2.7 Tg/year for acetone. CO biomass
237 burning emissions in Southeast Asia account for 7 Gg/month in spring, while up to 15 Gg/month
238 were reported from Carmichael et al. (2003). The anthropogenic and biomass burning emissions
239 of SO₂ (total of 142 Tg/year), BC (7.7 Tg/year) and OC (66.1 Tg/year) are based on the
240 AEROCOM emission inventory (Dentener et al., 2006), also representative of the year 2000. The
241 biogenic NMVOC emissions are calculated on-line with the MEGAN module of Guenther et al.
242 (2006). The simulated global annual mean emission of biogenic NMVOCs between 1995 and
243 2004 is 830 Tg(C)/year, isoprene contributes by 57 %, followed by terpenes (21 %), methanol
244 (12 %), and other NMVOCs such as acetaldehyde (2.5 %) and acetone (2.3 %). Other natural
245 emissions calculated on-line by the model are the Dimethyl Sulfide (DMS) fluxes (Kettle and

246 Andreae, 2000; Nightingale et al., 2000; Pham et al., 1995), sea salt aerosols (Schulz et al., 2004)
247 from the oceans, and mineral dust aerosols (Tegen et al., 2002; Cheng et al., 2008).

248 Our base year for aerosol and trace gas emissions is 2000, and emissions were repeated
249 annually throughout the simulation period. One point to note is that there were substantial
250 emission changes in Asia and Africa (increasing trends) and Europe and North America
251 (decreasing trends) during the study period, which is not captured in our simulations. A
252 consequence of these emission changes for our study would be that we may underestimate the
253 impact from local pollution sources on PAN concentrations in the UTLS over the ASM region in
254 recent years and that we overestimate the contribution from long-range transport of northern
255 hemispheric pollution. We provide an estimate of this error in the discussion of the results.
256 Lightning NO_x emissions are parameterized following Grewe et al. [2001]. They are proportional
257 to the calculated flash frequency with a production rate of 9 kg(N) per flash, and distributed
258 vertically using a C-shaped profile. The calculated flash frequency is resolution-dependent and
259 scaled globally to yield annual global emissions of 3.4 Tg(N) per year. To study the impact of
260 lightning on the distributions of PAN we compare two sets of experiments; each conducted for
261 11 years 2000-2010: (1) the control experiment (CTRL) and (2) the lightning off experiment
262 (light-off).

263 Model simulated PAN, NO_x , HNO_3 and O_3 mixing ratios are evaluated with
264 climatological datasets of airborne campaigns during the monsoon season (June-September). The
265 data were retrieved from <http://acd.ucar.edu/~emmons/DATACOMP/CAMPAIGNS/> (see also
266 the paper by Emmons, 2001). The NO_x and ozone volume mixing ratios observed during Cloud
267 Aerosol Interaction and Precipitation Enhancement Experiment (CAIPEEX) (details available in

268 Kulkarni et al., 2012), September 2010, are evaluated over the Indian region. The details of
269 instruments and measurement techniques are available at
270 <http://www.tropmet.res.in/~caipeer/about-data.php>. The list of data sets and aircraft campaign
271 used for comparison are presented in Table 1. For the comparison, aircraft observations are
272 averaged over 0 - 2 km, 2 - 6 km and 6 - 8 km and horizontally over the coherent flight regions.

273 In order to understand the impact of NO_x and NMVOCs emissions on the distribution of
274 PAN, we conducted a reference and 3 emission sensitivity simulations for the year 2003 driven
275 by European Centre for Medium-Range Weather Forecasts operational analyses (Integrated
276 Forecast System (IFS) cycle-32r2) meteorological fields (available every 6 h) (Uppala et al.,
277 2005). Model simulations were performed for the year 2003 since there was no significant
278 oceanic/meteorological perturbation event like, e.g., El Niño Southern Oscillation or the Indian
279 Ocean Dipole (http://www.marine.csiro.au/~mcintosh/Research_ENSO_IOD_years.htm). In
280 experiments 1 to 3, emissions of both NO_x and MNVOCs were simultaneously reduced by
281 10% over (1) Asia (10°S - 50°N , 60°E - 130°E), (2) Africa (30°S - 30°N , 15°W - 45°E), and (3)
282 North America (15°N - 45°N , 120°W - 75°W) separately, refereed as Asia-10%, Africa-10%,
283 North-America-10%.

284 **2.3 Model production of PAN**

285 PAN is a secondary pollutant that has a short lifetime in the lower troposphere. This reduces the
286 number of source points that contribute to PAN concentrations at any location in the UTLS
287 resulting in a clearer identification of source-receptor pathways. Figure 1 shows the distribution
288 of PAN production at 14 km and 16 km. A striking feature is the confinement of PAN production
289 to regions of deep convection. A maximum daily production rate of PAN in the UTLS, in these

290 convective zones, is >24 ppt/day near 14 km and >12 ppt/day near 16 km. Production of PAN
291 from background concentrations of ethane (C₂H₆) and other NMVOCs outside of deep
292 convection regions is distinctly secondary. NMVOCs are subject to the same convective
293 transport as NO_x and PAN formation occurs where both have the highest values. The lifetime of
294 NO_x is short throughout the troposphere which implies that PAN production in the UT can be
295 associated with deep convection. There is also a contribution to PAN production from
296 stratospheric air penetrating into the troposphere (Liang et al., 2011). Tropopause folding is a
297 significant source of exchange between the stratosphere and the troposphere (Gettelman et al.,
298 2011). This is an extratropical process that likely contributes to the PAN formation maxima over
299 North America, Europe and Asia shown in Figure 1(a) via enhanced conversion of ethane. In the
300 model it is unable to obscure the relationship between PAN formation and NO_x pollution source
301 regions.

302 **3. Comparison of model simulations with observations**

303 **3.1 Comparison with aircraft measurements**

304 Figure 2 shows scatter plot between aircraft observations and model simulations at the coherent
305 locations. Both aircraft observations and model simulations are averaged for the monsoon season
306 and altitude ranges. It indicates that model simulated PAN, O₃ and NO_x show good agreement
307 with aircraft measurements, correlation coefficient >0.7 and significance (P-value) varies
308 between 0.00 to 0.3 indicating correlation is significant at 95% confidence level. However
309 simulated HNO₃ between 2 - 6 km and 6 -10 km does not agree well with aircraft observations.

310 A point to point comparison of (latitude-longitude transects at various altitudes) simulated PAN,
311 NO_x, O₃ and HNO₃ (for the period 1995-2005) with aircraft observations are presented by

312 Fadnavis et al. (2014). These plots show good agreement between model simulations and aircraft
313 observations. Vertical variation of simulated ozone also shows good agreement with ozonesonde
314 measurements over India (see supplementary figure S3 in Fadnavis 2014). It should be noted that
315 current model simulations (2000-2010) show better agreement with aircraft observations than
316 Fadnavis et al., (2014). Figures showing the difference between these simulations and the aircraft
317 observations are provided in the supplement as Figure S2. The model bias varies with species
318 and altitude. In general, the bias in PAN is ranging from -20 ppt to 80 ppt, for ozone from -2ppb
319 to 40 ppb, for HNO₃ from -20ppt to 75 ppt while NO_x mixing ratios show a good agreement with
320 CAIPEEX measurements over the Indian region. Unfortunately, there were no measurements of
321 PAN or HNO₃ made during CAIPEEX.

322

323 **3.2 Comparison with MIPAS-E retrievals**

324 In order to study the influence of monsoon circulation on the distribution of PAN in the
325 UTLS region, multi-year averages (2005-2011) of seasonal mean (June-September) PAN
326 retrievals from MIPAS-E are analyzed. Figure 3 (a) presents these data for the altitude range 14 -
327 16 km, and Figure 3 (b) shows the corresponding ECHAM5-HAMMOZ results for comparison.
328 MIPAS-E observations show maximum PAN mixing ratios (~200 - 230 ppt) over (1) the Asian
329 monsoon anticyclone region (12^o - 40^o N, 20^o - 120^o E), and (2) over parts of North America,
330 the Gulf Stream, (3) southern Atlantic Ocean and west coast of tropical Africa. ECHAM5-
331 HAMMOZ CTRL simulations also show high PAN concentration at these locations, however
332 PAN concentrations are lower than MIPAS-E observations and appear somewhat more localized.
333 MIPAS-E exhibits a PAN maximum originating from African sources over the South Atlantic,
334 whereas the model shows this maximum over the African continent. This may be the outflow of

335 biomass burning over central and southern Africa during summer monsoon, which might be
336 underestimated in the model. The biomass burning region of Africa during the ASM season is
337 $\sim 30^{\circ}\text{S} - 20^{\circ}\text{N}$; $20^{\circ}\text{W} - 30^{\circ}\text{E}$ (Glanter et al., 2000). The longitude-altitude and latitude-altitude
338 cross-sections of MIPAS-E observed and simulated PAN over the biomass burning region are
339 plotted in figure S3. Model simulation shows that the biomass plume rising from Africa move
340 westward and northward over the Atlantic Ocean and merges with South American plume. From
341 satellite, aircraft observations and model simulations Real et al., (2010), and Barret et al., (2008)
342 reported a plume in the mid and Upper Troposphere (UT) over the southern Atlantic which
343 originates from central African biomass burning fires.

344 The difference between ECHAM5-HAMMOZ simulation and MIPAS observations are
345 shown in figures S3 (c) and S3 (f). These figures show that the model underestimates biomass
346 burning PAN by 20 - 60 ppt. These differences may also be related to issues in the vertical
347 transport of PAN, or to a possible underestimation of the emission sources of NMVOCs.
348 Uncertainties in the rate coefficients and absorption cross sections of PAN may also play a role.
349 Furthermore, anthropogenic NO_x emissions are mostly underestimated in the emission
350 inventories (Miyazaki et al., 2012). As discussed in Fadnavis et al. (2014), UTLS PAN over the
351 ASM is sensitive to NO_x emission changes in India or China. In their study, also performed with
352 ECHAM5-HAMMOZ, a 73 % NO_x emission change in India lead to a PAN increase of 10 - 18
353 %, while a 73 % NO_x emission change in China changed PAN over the ASM by 18 - 30 %. The
354 cross-section plots of (see figure S4) differences in MIPAS-E PAN with model simulated PAN
355 indicate that in the UTLS, MIPAS-E PAN is higher than model simulated PAN by $\sim 20 - 60$ ppt
356 (except at 20 km). PAN is lower by 20 - 40 ppt over eastern part of ASM anticyclone (Southern
357 India and South East Asia) and also over Indonesia and northern Australia. In general, in the

358 ASM region, during the monsoon season, MIPAS-E PAN is higher than model by 30 - 60 ppt
359 between 8 - 16 km and the difference between MIPAS-E and model PAN vary between +40 ppt
360 to -40 ppt between 17 and 20 km.

361

362

363 **4. Transport of PAN during monsoon season**

364 **4.1 Transport from Northern tropical land mass**

365 Figure 3(a) shows high concentrations of MIPAS-E PAN at 14-16 km over Asia, North
366 America and tropical Africa. ECHAM5-HAMMOZ simulations (figure 3b) also show similar
367 distribution. This may be due to transport from boundary layer into the UTLS by the monsoon
368 convection from respective regions. ECHAM5-HAMMOZ simulated OLR and 850hpa winds
369 averaged for the monsoon season are shown in Figure S5(a). They indicate the extent of deep
370 convection near the surface. NECP reanalysis OLR and 850 hPa winds averaged for monsoon
371 season (2000-2010) are plotted in figure S5 (b) for comparison. These figures indicate that the
372 model can reproduce deep convection as well as the large scale circulation. Cross-section of
373 distribution of simulated Cloud Droplet Number Concentration (CDNC) and ice crystal number
374 concentration (ICNC) over Asia, North America and tropical Africa confirms strong convective
375 transport from these regions (figure S5 (c)-(e)). It should be noted that vertical velocities in a
376 large scale model also indicate rapid uplift in deep convective regions. From satellite
377 observations and model simulations Park et al., (2009) reported transport of fraction of boundary
378 layer carbon monoxide (CO) into the UTLS by the Asian monsoon convection.

379 To illustrate vertical transport, longitude-altitude cross sections of PAN mixing ratios
380 averaged over the region 0° - 30° N for June-September as obtained from MIPAS-E and

381 ECHAM5-HAMMOZ are shown in Figures 4(a) and (b) respectively. Both MIPAS-E
382 observations and ECHAM5-HAMMOZ simulations show elevated levels of PAN (200 - 250 ppt)
383 near 80° E - 100° E (ASM), 30° W - 30° E (WAM) and 80° W - 100° W (NAM) region. The
384 simulated PAN distribution along with winds plotted in Figure 4(b) show cross tropopause
385 transport from these regions. It reveals that transport of boundary layer PAN to the UTLS mainly
386 occurs from strong convective regions, i.e. Bay of Bengal (~80° E - 90° E), South China Sea
387 (~100° E - 120° E), western Atlantic Ocean (Gulf Stream region) and Gulf of Mexico (80° W -
388 100° W). MIPAS-E observations and model simulations show that the transport due to ASM is
389 strongest and reaches deepest into the lower stratosphere. This is due to the more intense deep
390 convection activity over the ASM region compared to the NAM region (see figure S5 (c)-(e)).
391 Figure 4(c) presents the differences between MIPAS and model simulated PAN. It appears that
392 the model PAN is overestimated over the ASM (20 - 30 ppt) and underestimated over the NAM
393 (50 - 70 ppt) and WAM (20 - 50 ppt) regions between 8km and 18km. However, the
394 overestimation in the UT in the ASM is difficult to explain on physical grounds and is more
395 likely to be a MIPAS-E sampling issue as discussed later.

396 **4.2 Transport from southern tropical land mass**

397 In order to understand transport of PAN due to southern WAM, SAM and AUSM, we show
398 longitude-pressure sections of MIPAS-E observations and model simulated PAN concentrations
399 averaged over 0° - 25° S in Figure 4(d)-(e) respectively. The model has plumes near 20° E, 100°
400 E and 80° W. These three regions of convective transport are (1) tropical southern Africa 10 -40°
401 E, referred to as South Africa, (2) Indonesia and northern parts of Australia ~100° -110° E and
402 (3) South America ~70° - 80° W. Outflow from Indonesia and from northern parts of Australia

403 (~100° E) penetrates deep into the UTLS. Tropical Rainfall Measuring Mission (TRMM)
404 satellite observations show high frequency of intense overshooting convection over these areas
405 (during the monsoon season) with highest density in the belt 0° - 10° S over the Caribbean,
406 Amazon, Congo and Southern Maritime Continent (Liu and Zipser, 2005). The analyses of
407 vertical winds show strong transport from 10° - 40° E, 100° - 110° E, 70° - 80° W (in the belt 0° -
408 10° S) (figure not shown). The amount of high level cloud fraction is also high over these
409 regions. Distribution of CDNC and ICNC show deep convection over these regions (Figure not
410 shown). The model simulations show high PAN concentrations reaching the UTLS. Thus
411 transport due to deep convection is reasonably well captured by the model. However, the
412 MIPAS-E retrievals only show a plume rising over South Africa and no enhancement over the
413 AUSM (Indonesia-Australia) and SAM regions. Figure 4(e) shows that the plumes from the three
414 outflow regions are mixed in the UT (8 - 14 km) by the prevailing westerly winds. The reasons
415 for a single plume seen in MIPAS-E may be that lower concentrations of PAN reach these
416 altitudes (above 8 km) from SAM and AUSM and mix with the plume over South Africa. There
417 are indications of elevated PAN concentrations at the lower boundary in Figure 4 (d).
418 Simulations show lower PAN mixing ratios over the longitudes of SAM and AUSM (see figure
419 4(e)). The differences between MIPAS observations and simulations (figure 4(f)) show that
420 model PAN is overestimated in the AUSM (10-30ppt) and is underestimated over the southern
421 WAM (20 - 70 ppt) and SAM (20 - 50 ppt) between 10 km and 18km. It is likely that the three
422 plume structure in the UT seen in model is being obscured in the observations due to sampling
423 issues since periods of deep convection reaching significantly above 8 km are associated with
424 significant cloud cover.

425 Figure 4 shows that simulated transport of PAN due to ASM, NAM and WAM convection
426 are stronger and penetrate deeper into the UT compared to SAM and AUSM. This is consistent
427 with the distribution of deep convection noted by Gettelman et al. (2002). In general, the PAN
428 amounts in the UTLS in the model are less than those observed by MIPAS-E. This may be due
429 to an underestimation of the chemical PAN source from VOC precursors or too little vertical
430 transport in the model or a combination of both. Earlier model studies with ECHAM also
431 exhibited too low concentrations of CO in the upper tropospheric outflow (M. Schultz,
432 unpublished data from the NASA Global Tropospheric Experiment TRACE-P mission).

433 **4.3 Transport from Asian Summer Monsoon region**

434 The ASM anticyclone extends from 60°E to 120°E and 10°N to 40°N (see figure 3 (b)).
435 Latitude-altitude cross sections over the ASM anticyclone (60° E - 120° E) of MIPAS-E
436 observed PAN (plotted in the altitude range 8 - 20 km) and ECHAM5-HAMMOZ CTRL
437 simulations are shown in Figures 5(a) and (b), respectively. ECHAM5-HAMMOZ simulations
438 are similar to MIPAS-E retrievals of PAN. There is indication of plume ascent into the lower
439 stratosphere. The ECHAM5-HAMMOZ simulations also show transport of subtropical boundary
440 layer PAN into the UTLS due to deep convection. This is not visible in the MIPAS-E data
441 because of the lack of data below 8 km. Figure 5 (b) shows that there is transport from 40° - 50°
442 N reaching up to 10 km (~200 hPa). Park et al. (2004, 2007, 2009) and Randel and Park (2006)
443 noted that trace species are introduced into the monsoon anticyclone at its eastern end around
444 200 hPa. The uplift over south-east Asia and the base of the Himalayas in India pumps tracers
445 into the upper tropical troposphere where they get horizontally redistributed by the anticyclonic
446 circulation and form the region of high PAN values between 40° N and high latitudes. Figure

447 10(c) shows that the mid-latitude maximum seen in Figure 5(c) is due to pollution transport from
448 Europe. The Chinese emissions are feeding into this large plume over Russia and are transported
449 partly and diluted over the extratropical Pacific Ocean. The latitude-altitude section of
450 differences between MIPAS and simulated PAN indicates that ASM plume is underestimated in
451 the model (see figure 5 (c)). It is interesting to compare figure 4(c) (longitude –altitude section)
452 and figure 5(c) (latitude-altitude section). The reason for underestimation of the ASM plume in
453 the latitude-altitude section may be due to a lower contribution from the eastern part of
454 anticyclone in the model. Figure S4 shows model PAN is underestimated over Southern India
455 and South East Asia in the UT and overestimated in the lower stratosphere.

456 In order to understand the impact of transport from ASM region on the rest of the world,
457 we analyze differences between reference and Asia-10% simulations (reference –Asia-10%).
458 The latitude-altitude and longitude-altitude cross sections over the ASM region (Figures 5 (d)
459 and 5(e)) show transport of ~5-20 ppt of PAN into the lower stratosphere. The horizontal cross
460 sections at 14 km to 21 km (figures 5 (f) – 5(i)) show that Asian PAN is transported to northern
461 Atlantic by subtropical westerly winds. These figures show that a 10% change in Asian
462 emissions (NO_x and NMVOCs) transports ~5-30 ppt into the UTLS over Asia and 1-7 ppt of
463 PAN in the UTLS of Northern subtropics and mid latitudes.

464 4.4 Transport from North American monsoon region

465 Figures 6(a) and (b) exhibit latitude-altitude sections of PAN from MIPAS-E retrievals and
466 ECHAM5-HAMMOZ simulations (seasonal mean for July-September) over the North American
467 monsoon region between 70° W - 120° W. MIPAS-E observations and the model indicate

468 transport of PAN into the UTLS. The distribution of ECHAM5-HAMMOZ simulated PAN from
469 the boundary layer to UTLS shows the source region is at around 40^o N. There is convective
470 uplift of PAN over the northern Gulf of Mexico region and over the Gulf Stream. High amount
471 of pollutants emitted from north east America from a number of power plants are located in
472 Atlanta, Washington, Chicago, Boston, Jacksonville (CEC report, 2011). The tropospheric NO₂
473 columns retrieved from the SCIAMACHY and OMI satellite instrument shows high amounts of
474 anthropogenic NO₂ emissions over this region (Lamsal et al., 2011, Miyazaki et al., 2012). The
475 model simulations show high amount of PAN concentrations over this region (see figures 10(a)-
476 (d)). The monsoon convection lifts these pollutants to the UT. The outflow of these pollutants is
477 over the Atlantic (see figures 3 (a)). TRMM precipitation radar observations show significant
478 overshooting convective activity over this region during the monsoon season (Liu and Zipser,
479 2005). The vertical distribution of differences in MIPAS and simulated PAN shows that PAN is
480 underestimated in the model (see figure 6(c)) over North and South America (10-60 ppt) between
481 10-18km, however PAN is overestimated in the model between 8-10km in the region near 30^oN .
482 As discussed above this may be associated with European emissions and transport.

483 Figures 6 (d) - 6 (e) show impact of North American emission (reference – North-America-10%)
484 on the transport of PAN. The figure shows cross tropopause transport of PAN by North
485 American monsoon convection. The amount of PAN transported (~1-5 ppt) into the lower
486 stratosphere is less than for the ASM (~10-20 ppt). The latitude-longitude distribution of PAN
487 (figures 6 (f) – 6(i)) shows that the upper tropospheric westerly winds transport ~1-10 ppt of
488 PAN to Atlantic, Europe and North China.

489

490 **4.5 Transport from West African region**

491 Figures 7 (a) - (b) show vertical distributions of PAN over the African region (averaged
492 over 0° - 45° E). MIPAS-E observations and model simulations indicate a plume that crosses the
493 tropopause and enters the lower stratosphere. The model surface fields (see Figure 7(b)) show
494 that this plume arises from latitudes 5 - 20° S over Africa and that it moves equatorward. It
495 subsequently merges with the ASM plume. A prominent tongue of high PAN values between
496 30° and 60° N is captured in model simulations. This feature appears to be related to emissions
497 from Europe being transported towards the equator in the upper subtropical troposphere.
498 However, in the model, emissions from Europe are transported poleward instead of equatorward
499 (Figure 7(b)). There is a region of strong descent in the model between 30° N and 40° N (see
500 Figure 7(b)) which deforms the PAN isopleths around 12 km around 30° N. This feature is not
501 seen in the MIPAS-E retrievals and indicates a disagreement of the model with the transport
502 pattern of the atmosphere in this region. The transport of PAN in the 10° - 20° S latitude band
503 over the Congo, Angola, Tanzania regions of southern and tropical Africa is not pronounced in
504 the model compared to MIPAS-E observations. This behavior indicates that deep tropical
505 convection is underestimated in the model in this latitude band. The vertical distribution of
506 differences in MIPAS and simulated PAN (figure 7(c)) shows that simulated PAN is
507 underestimated over these regions (5° - 20° S and 20° - 40° N) between 10 km and 18 km. The
508 reason may be related to underestimation of deep tropical convection in the model in this latitude
509 band. Simulated PAN is overestimated between 8km and 12km near the equator.

510 The reference - Africa-10% simulation (figures 7(d)-7(e)) shows that African PAN is
511 transported up to the tropopause. The cross sections over North and South Africa show

512 penetration of North African plume into the lower stratosphere (~19km). However, PAN
513 transport into the lower stratosphere (~0.2-0.6 ppt) is comparatively less than Asia or North
514 America. Figures 7 (g) - 7(j) show transport of ~5-50 ppt of PAN in the UT (6-12km) of tropical
515 Africa. There is transport from equatorial Africa to Atlantic and Mexico between 6-8km (figures
516 7 (g) – 7 (h)) which is then transported to North China by upper tropospheric (12km) westerly
517 winds (see figures 7 (j)).

518 The model simulated latitude-altitude, longitude-altitude cross sections of NO_x , and
519 HNO_3 over the ASM ($10^\circ\text{N} - 40^\circ\text{N}$, $60^\circ - 120^\circ\text{E}$), NAM ($10^\circ\text{N} - 40^\circ\text{N}$, $70^\circ\text{W} - 120^\circ\text{W}$) and
520 WAM ($0^\circ - 25^\circ\text{S}$, $0^\circ - 45^\circ\text{E}$) are shown in Figures 8 (a) – 8(j), respectively. Figures 8 (a)- 8(e)
521 show transport features of NO_x . These are similar to those seen in the distribution of PAN, but
522 with sharper signatures due to the shorter lifetime of NO_x . This shows that monsoon convection
523 lifts boundary layer pollutants including NO_y species to the UTLS. The distribution of HNO_3
524 (see Figures 8 (f) - 8(j)) shows a complex pattern. Comparing Figure 4(b), the region around
525 100°E with intense convective uplift corresponds to HNO_3 depletion from the surface to above
526 10 km. In fact, the upper tropospheric region of the ASM anticyclone exhibits much lower values
527 of HNO_3 compared to all the other longitudes in the $10^\circ - 40^\circ\text{N}$ band (Figure 8(h)). This
528 suggests that in the model the convective transport in the ASM region is associated with efficient
529 removal by wet scavenging. In contrast, the North American monsoon region has HNO_3
530 ascending to the UT with significantly less loss. This is likely due to the fact that convection
531 involved in vertical transport during the NAM is not as intense and not as deep as in the case of
532 the ASM and there are differences in wet scavenging. Figure 8(g) shows that the plume rising
533 from South America moves towards the equator but does not have the extension into the UT as
534 the North American plume. These are June-September averages and the ITCZ is on the northern

535 hemisphere side during this period. Thus, weaker convective transport is to be expected on the
536 southern hemisphere side of the equator during this period. Figure 8 (i) shows significant
537 transport of African emissions around $\sim 0^{\circ}$ - 15° S and a plume rising from Europe ($\sim 35^{\circ}$ N - 60°
538 N) as well.

539 Figures 9 (a) –9 (f) show vertical distribution of HNO_3 and O_3 , over Asia, North America
540 and Africa as obtained from differences between the reference and Asia-10%, reference and
541 North-America-10% as well as reference and Africa-10% simulation. It is evident that transport
542 of HNO_3 for Asia-10% simulation is deeper in the UT ($\sim 16\text{km}$) than North-America-10% and
543 Africa-10% simulations. It can be seen that Asia-10%, North-America-10% and Africa-10%
544 simulations transport $\sim 7\text{-}10$ ppt, $\sim 5\text{-}7$ ppt and $\sim 3\text{-}5$ ppt of HNO_3 in the UT of their respective
545 regions.

546 In the UT, between 6km and 10km, Asia-10% simulation shows transport of $\sim 10\text{-}15$ ppt
547 of HNO_3 over Western Pacific and $\sim 3\text{-}10$ ppt over tropical America by the subtropical westerly
548 winds (figure not included). North-America-10% simulation shows transport of $\sim 5\text{-}7$ ppt of
549 HNO_3 over Atlantic, North Africa, Saudi Arabia and North China by the subtropical westerly
550 winds and $\sim 3\text{-}5$ ppt of HNO_3 over equatorial pacific, Indonesia, China and India by the tropical
551 easterly winds. Africa-10% simulation shows transport of $\sim 3\text{-}5$ ppt HNO_3 from North Africa to
552 North America, equatorial pacific, also there is transport of ~ 4 ppt of HNO_3 from South Africa to
553 Atlantic, South America, Indonesia, China and India by the tropical easterly winds (figure not
554 included).

555 North-America-10% simulation shows transport of boundary layer ozone extending up to
556 the tropopause, which are higher than for the Asia-10% and Africa-10% simulations (figures 9

557 (d) – 9 (f)). Asia-10%, North-America-10% and Africa-10% simulations show transport ~1-2
558 ppb, ~0.8-1.5 ppb and ~0.4-0.6 ppb of ozone in the UT of their respective regions.

559 In the UT, between 6km and 10 km, Asia-10% simulation shows transport of ozone ~1.5
560 ppb to Western Pacific and 0.8 ppb to Mexico and United States by the subtropical westerly
561 winds (figure not included). North-America-10% simulation shows transport of 0.4-1.5 ppb of
562 O₃ to equatorial Pacific extending up to Indonesia by the tropical easterly winds. There is some
563 outflow (~0.6ppb) over Atlantic by the subtropical westerly winds as well (figure not included).
564 Africa-10% simulation shows transport of ~0.4-0.8 ppb of ozone to equatorial Atlantic and
565 Mexico (figure not included).

566 It can be seen that similar emission change over Asia, North America and Africa causes
567 highest change in HNO₃ and Ozone in the UT over Asia and least over Africa. In the UT,
568 between 6km and 10 km, transport of HNO₃ by Asia-10% (~3-10 ppt of HNO₃ to tropical
569 America) is higher than North-America-10% (~3-7 ppt of HNO₃ to China and India) and Africa-
570 10% (~3-5 ppt of HNO₃ to tropical America, China and India). Similarly ozone transport is
571 higher for Asia-10% than North-America-10% and Africa-10% simulations.

572

573 **4.6 Horizontal transport**

574 PAN concentrations from MIPAS-E and ECHAM5-HAMMOZ at different altitudes are
575 analyzed to investigate horizontal transport. Figure 10(a) shows the distribution of PAN from
576 ECHAM5-HAMMOZ simulations near the surface (2 km). Sources of PAN are apparent over
577 South America, southern Africa, North America, Europe, Russia and northern China/Mongolia.
578 The PAN distribution at 4 km (see Figure 10(b)) shows high concentrations above these regions
579 indicating vertical transport. Figures 10(c) and 10 (d) show the distribution at 6 km and 8 km.

580 The upper level anticyclonic circulation between 10^o N and 30^o S over the Atlantic transports
581 PAN from central Africa towards America and from Brazil towards southern Africa. The large
582 Scale Biosphere-Atmosphere Regional Experiment in Amazonia (LBA-CLAIRE-98) campaign
583 observations (Andreae et al., 2001) and African Monsoon Multidisciplinary Analysis (AMMA)
584 project (Real et al., 2010) show that the biomass burning plume originating from Brazil is lifted
585 to altitudes around 10 km. This plume is entrained into deep convection over the northern
586 Amazon, transported out over the Atlantic and then returned to South America by the circulation
587 around a large upper-level anticyclone. This transport is well captured by the model.

588 North American pollution is also being transported by the westerly winds over Eurasia,
589 forming an organized belt. This transport pattern persists up to 12 km (Figure 10 (e) and 10(g)).
590 MIPAS-E observations at 12 km also show this transport pattern. The source region for the PAN
591 from southern Africa is the region of active biomass burning. Since this region is located in the
592 tropics, the outflow is over the Atlantic due to the prevailing easterly winds. ECHAM5-
593 HAMMOZ simulations show similar transport (see Figures 10(e)). But there are differences; in
594 particular the transport over tropical Africa does not get displaced over the Atlantic Ocean. As
595 noted above, there are significant transport differences between the model and observations in
596 this longitude band. Another difference is that PAN is not transported westward over Central
597 America and towards the Pacific Ocean.

598 Figures 10(f)-10(h) show the distribution of PAN from ECHAM5-HAMMOZ
599 simulations and MIPAS-E retrievals, in the lower stratosphere (18 km). In both data sets PAN
600 is transported westwards from ASM, NAM and WAM by prevailing easterly winds and
601 maximizes in the region of the ASM anticyclone.

602 As can be seen from the above discussions, the ASM, NAM, and WAM outflow and
603 convection over the Gulf Stream play an important role in the transport of boundary layer
604 pollution into the UTLS. Previous studies (e.g. Fadnavis et al., 2013) indicated that over the
605 Asian monsoon region, transport into the lower stratosphere occurs and there is significant
606 vertical transport over the southern slopes of the Himalayas (Fu et al., 2006, Fadnavis et al.,
607 2013) and also over the region spanned by the Bay of Bengal and the South China Sea (Park et
608 al., 2009). Pollutant transport due to North American convection and tropical African outflow
609 does not penetrate as deep into the stratosphere as the ASM. However there is clear indication
610 that in the UT, middle latitude westerly winds connect the North American pollution to the
611 ASM.

612 Figures 3-7 and figure 10 show that in the UT, westerly winds drive North American and
613 European pollutants eastward to at least partly merge with the ASM plume. Strong ASM
614 convection transports these remote and regional pollutants into the stratosphere. The Caribbean
615 is a secondary source of pollutant transport into the stratosphere. In the stratosphere the injected
616 pollutants are transported westward by easterly winds and into the southern subtropics by the
617 Brewer-Dobson circulation.

618

619 **5.0 Impact of Lightning on tropospheric PAN, NO_x, HNO₃ and ozone**

620

621 In the ASM region and during the monsoon season the NO_x released from intense lightning
622 activity enhances the formation of PAN, HNO₃ and ozone in the middle and upper troposphere
623 which is already relatively strong due to the intense solar radiation along with high background
624 concentrations of NO_x, HO_x and NMVOCs (Tie et al., 2001). PAN, HNO₃ and O₃ produced from

625 lightning may get transported in the lower stratosphere by deep monsoon convection and
626 contribute to anthropogenic emission transport of these species. In order to understand
627 contribution of lightning and the dominating lightning production regions, we analyze difference
628 between control and light-off simulations. Figure 11(a)-(d) shows the percentage changes in
629 model simulated ozone, HNO₃, PAN and NO_x due to lightning as zonally averaged spatial
630 distribution of seasonal mean (June-September) mixing ratios. The analysis indicates that the
631 impact of lightning on these species is largest in the tropical UT between 40° N -40° S and
632 between 8 km and 14 km. In the tropical mid troposphere lightning produced maximum ozone is
633 ~15 – 25 % (12 - 24 ppb) , HNO₃ ~ 40 – 60 % (50 -90 ppt) ~ PAN ~15 – 25 % (70 - 140 ppt) and
634 NO_x ~20 – 40 % (10 - 35 ppt) while in the UT ozone is ~20 -30 % (20 - 28 ppb), HNO₃ ~60 -
635 75% (80 - 110 ppt), PAN ~28 – 35 % (120 - 170 ppt), and NO_x ~50 – 75 % (20 - 65 ppt). Our
636 results are consistent with model simulations by Tie et al., (2001) and Labrador et al. (2005). The
637 spatial distributions of NO_x, ozone, PAN and HNO₃ produced from lightning (see figures 12 (e)
638 – (h)) indicate that in the UT (12 km) increases in O₃ ~20 - 25 % (11 - 17 ppbv), HNO₃ ~40 – 70
639 %, PAN ~25 – 35 % and NO_x ~55 - 75 %, over North America are in agreement with previous
640 studies (e.g Labrador et al., 2005; Hudman et al. 2007; Zhao et al., 2009; Cooper et al., 2009),
641 over equatorial Africa (PAN 30 - 45 %, HNO₃ ~70 - 80 %, O₃ ~ 25 %, NO_x~70 %) agrees well
642 with Barret et al., 2010; Bouarar et al., 2011 and over the ASM region (PAN ~ 25 %, HNO₃ ~65
643 -70 %, O₃ ~20 %, NO_x ~ 60 - 70 %) agrees with Tie et al., (2001). These regions coincide with
644 regions of convective vertical transport of PAN (as seen in figures 4 and 5). Lightning produced
645 PAN will be lifted into the lower stratosphere by the monsoon convection along with
646 anthropogenic emissions and will redistribute in the tropical lower stratosphere. Latitude-
647 longitude cross sections of lightning induced PAN, NO_x, ozone and HNO₃ formation at altitudes

648 between 8 - 14 km show that the production of PAN, NO_x, ozone and HNO₃ is less over the
649 ASM region than over the equatorial Americas and Africa (also seen in figure 11). The high
650 amounts of PAN over the ASM are therefore primarily due to anthropogenic emission transport
651 into the UTLS from the source regions in Southern and Eastern Asia. As discussed in Fadnavis
652 et al., 2014, NO_x emissions are estimated to have changed by 38 % in India and 76 % in China,
653 respectively during 2002 - 2011 period. From sensitivity simulations they deduced corresponding
654 changes in upper tropospheric PAN are > 40 %, O₃ by > 25 % and HNO₃ by > 70 % over the
655 Asian monsoon region. These effects are larger than the impact of lightning NO_x emissions over
656 this region (figure 11 (e)-(h)).

657

658 **6. Conclusions**

659 In this study statistical analysis of simulated and satellite-retrieved mixing ratios of PAN,
660 NO_x, and HNO₃ is presented in order to determine the transport patterns of pollution into the
661 Asian monsoon region and the impact of pollution flowing out of the ASM into other regions of
662 the global atmosphere. The analysis focused on the upper troposphere and lower stratosphere and
663 covered the period 2002 - 2011. In ECHAM5-HAMMOZ simulations both NO_x and NMVOCs
664 emission were simultaneously reduced by 10% over ASM, NAM and WAM to understand
665 transport pathways and their relative contribution the UTLS. As discussed in Fadnavis et al.
666 (2014), NO_x emissions are estimated to have changed by 38 % in India and 76 % in China,
667 respectively during this period. From sensitivity simulations they deduced corresponding
668 changes in upper tropospheric PAN > 40 %, O₃ by > 2 5% and HNO₃ by > 70 % over the ASM
669 region. These effects are larger than the impact of lightning NO_x emissions over this region
670 discussed in section 3 of this study.

671 Interestingly, the ECHAM5-HAMMOZ reference simulation reveals that in the UT,
672 westerly winds drive North American and northward propagating South African pollutants
673 eastward where they mix with the ASM plume. Deep convection and strong diabatic upwelling
674 in the ASM, convectively transports a part of these plumes into the lower stratosphere. The
675 Caribbean region is another source of pollution transport into the stratosphere. Some cross
676 tropopause transport occurs due to convection over North America and Southern Africa as well.
677 In the lower stratosphere the injected pollutants from ASM, WAM and NAM are transported
678 westward by easterly winds and into the southern hemisphere subtropics by the Brewer-Dobson
679 circulation. The emission sensitivity simulations Asia-10%, North-America-10% and Africa 10%

680 confirm these transport pathways. In the southern hemisphere, plumes rising from convective
681 zones of South Africa, South America and Indonesia-Australia are evident in the model
682 simulations, but are not seen in the MIPAS retrievals. PAN concentrations are higher in the
683 plume rising from South Africa than SAM and AUSM. In the UT, they merge by the prevailing
684 westerly winds. MIPAS-E observations in the UTLS show a single plume over South Africa and
685 no enhancement over SAM or AUSM. The reasons for the single plume seen in MIPAS-E may
686 be that although there is uplifting by each of the three monsoon systems lower concentrations of
687 PAN reach these altitudes (above 8 km) from SAM and AUSM until they merge with South
688 African plume. It is also possible that the three plume structure in the UT seen in the model is
689 being obscured in the observations due to sampling issues. Convective cloud cover is strongly
690 associated with deep convection in the ASM region. The MIPAS-E data has a PAN minimum in
691 the UT right in the longitude band of the deep convection over the southern flanks of the
692 Himalayas (Figure 4(a)). This feature is unphysical and clearly identifies a sampling bias.
693 However, the model is also not fully reproducing the latitudinal structure of the PAN in the ASM
694 region UTLS which indicates that there are differences in both the distribution of convection and
695 the large scale circulation.

696 The horizontal transport of PAN analyzed from ECHAM5-HAMMOZ simulations show
697 that the PAN from southern Africa and Brazil is transported towards America by the circulation
698 around a large upper-level anticyclone and then lifted to the UTLS in the NAM region. This is
699 also evident in the Africa-10% simulation.

700 The vertical distribution of simulated HNO_3 over the monsoon regimes shows low
701 concentrations above 10 km at the foothills of the Himalayas. In contrast, the results show strong

702 uplifting of HNO₃ into the UT with NAM convection. This may be due to the fact that NAM
703 convection is not as intense as the ASM and there may be more wet removal of nitrogen oxides
704 in the ASM convection. The model simulations indicate a higher efficiency of NO_x conversion to
705 HNO₃ over the Indian region compared to NAM.

706 The change in emission (both NO_x and NMVOCs emissions were simultaneously
707 reduced by 10%) over each of ASM, WAM and NAM regions show that Asia-10% transport ~5-
708 30 ppt of PAN in the UTLS over Asia and ~1-10 ppt in the UTLS Northern subtropics and mid
709 latitude. North-America-10% simulation shows transport of ~1-5 ppt of PAN over Atlantic,
710 Europe and North China (between 12-14km) and 0.4-3ppt over Asia (near 16km). Africa-10%
711 simulation shows transport from equatorial Africa to Atlantic and North America between 6 – 8
712 km, which is then transported to Asia by upper tropospheric westerly winds (near 12km).

713 Transport of HNO₃ is deeper in the UT (~16km) in Asia-10% simulation than North-
714 America-10% and Africa-10% simulations. Asia-10%, North-America-10%, Africa-10%
715 simulations show transport of ozone ~1-2 ppt, 0.8-1.5 ppt and 0.4-0.6 ppt in the UT over
716 respective regions.

717 In the UT between 6km and 10km, transport of HNO₃ by Asia-10% (~3-10 ppt of HNO₃
718 to tropical America) is higher than North-America-10% (transport of 3-7 ppt of HNO₃ to China
719 and India) and Africa-10% (~3-5 ppt of HNO₃ to tropical America, China and India) simulations.
720 Similarly transport of ozone is higher for Asia-10% than North-America-10% and Africa-10%
721 simulations. Comparison of emission change over Asia, North America and Africa shows highest
722 transport of HNO₃ and ozone in the UT over Asia and least over Africa.

723

724 Lightning production of NO_x may enhance PAN concentrations in the UT and affect its
725 transport into the lower stratosphere. The percentage change in lightning produced ozone, HNO_3 ,
726 PAN and NO_x has been evaluated with a sensitivity simulation. In the UT, lightning causes
727 significant increases in these species over equatorial America, equatorial Africa and the ASM
728 region. These regions coincide with intense convective zones with significant vertical transport.
729 Lightning production is higher over equatorial Africa and America compared to the ASM.
730 However, the vertical distribution shows that higher amounts of PAN are transported into the UT
731 in the ASM region. This indicates that the contribution of anthropogenic emission to PAN in the
732 UTLS over the ASM, is higher than that of lightning. This is consistent with the fact that
733 anthropogenic emissions in the ASM region are higher than in the NAM and WAM (Lamsal et
734 al., 2011, Miyazak et al., 2012).

735

736 *Acknowledgements:* The authors thank the MIPAS-E teams for providing data and the High
737 Power Computing Centre (HPC) in IITM, Pune, India, for providing computer resources.
738 Authors are also thankful to anonymous reviewers and the Editor for their valuable suggestions.

739

740 References

- 741 Andreae, M. O., Artaxo, P., Fischer, H., Freitas, S. R., Grégoire, J.-M., Hansel, A., Hoor, P.,
742 Kormann, R., Krejci, R., Lange, L., Lelieveld, J., Lindinger, W., Longo, K., Peters, W.,
743 de Reus, M., Scheeren, B., Silva Dias, M. A. F., Ström, J., Velthoven, P. F. J. van and
744 William, J.: Transport of biomass burning smoke to the upper troposphere by deep
745 convection in the equatorial region, *Geophys. Res. Lett.*, 28, 951-958, 2001.
- 746 Arnold F. & Hauck G., Lower stratosphere trace gas detection using aircraft-borne active
747 chemical ionization mass spectrometry, *Nature*, 315, 307-309, |doi:10.1038/315307a0,
748 19 December 1984.
- 749 Aumann, H. H. and Ruzmaikin, A.: Frequency of deep convective clouds in the tropical zone
750 from 10 years of AIRS data, *Atmos. Chem. Phys.*, 13, 10795–10806, 2013.
- 751 Barret, B., Williams, J. E., Bouarar, I., Yang, X., Josse, B., Law, K., Pham, M., Flochmoen, E.
752 Le, Lioussé, C., Peuch, V.H., Calver, G.D., Pyle, J.A., Sauvage ,B., Velthoven P. van and
753 Schlager, H.: Impact of West African Monsoon convective transport and lightning NO_x
754 production upon the upper tropospheric composition: a multi-model study, *Atm. Chem.*
755 *Phys.*, **10**, 5719-5738, doi:10.5194/acp-10-5719-2010, 2010.
- 756 Barret B., Ricaud P., Mari C., Attié J.-L., Bousserez N., Josse B., Flochmoen E. LeLivesey N.
757 J., Massart S., Peuch V.-H., Piacentini A., Sauvage B., Thouret V., and Cammas J.-P.
758 Transport pathways of CO in the African upper troposphere during the monsoon season:
759 a study based upon the assimilation of spaceborne observations, *Atmos. Chem. Phys.*, 8,
760 3231–3246, 2008.

761 Barth, M., Lee, C. J., Hodzic, A. Pfister, G., Skamarock, W. C., Worden, J. , Wong, J., and
762 Noone, D.: Thunderstorms and upper troposphere chemistry during the early stages of the
763 2006 North American Monsoon, *Atmos. Chem. Phys.*, 12, 11003–11026, 2012.

764 Bouarar, I., Law, K. S., Pham, M., Liousse, C., Schlager, H., Hamburger, T., Reeves, C. E.,
765 Cammas, J.-P., Ned' el' ec' P., Szopa, S, Ravegnani, F., Viciani, S., D'Amato F.,
766 Ulanovsky A., and Richter A.: Emission sources contributing to tropospheric ozone over
767 Equatorial Africa during the summer monsoon, *Atmos. Chem. Phys.*, 11, 13395–13419,
768 doi:10.5194/acp-11-13395-2011, 2011.

769 Carmichael, G. R., Tang Y., Kurata G., Uno I., Streets D., Woo J.-H.,
770 Huang H., Yienger J., Lefer B., Shetter R., Blake D., Atlas E., Fried
771 A., Apel E., Eisele F., Cantrell C., Avery M., Barrick J., Sachse G.,
772 Brune W., Sandholm S., Kondo Y., Singh H., Talbot R., Bandy A.,
773 Thorton D., Clarke A., and Heikes B., Regional-scale chemical
774 transport modeling in support of the analysis of observations obtained
775 during the TRACE-P experiment, *J. Geophys. Res.*, 108(D21), 8823,
776 doi:10.1029/2002JD003117, 2003.

777 CEC (Commission for Environmental Cooperation) report on North American Power Plant Air
778 Emissions, IBSN : 978-2-89700-008-0, October 2011.

779 Chang, Chih-Pei, Ding Y., Lau, Gabriel Ngar-Cheung, Johnson, R. H, Wang, B., and Yasunari,
780 T.: *The Global Monsoon System: Research and Forecast (2nd Edition)* edited by Chih-
781 Pei Chang et al., World Scientific Publishing Co, 2011.

782 Choi, Y., Kim, J., Eldering, A., Osterman, G., Yung, Y. L., Gu, Y., and Liou, K. N.: Lightning
783 and anthropogenic NO_x sources over the United States and the western North Atlantic

784 Ocean: impact on OLR and radiative effects, *Geophys. Res. Lett.*, 36, L17806,
785 doi:10.1029/2009GL039381, 2009.

786 Collier J.C. and Zhang G.J.: Simulation of the North American Monsoon by the NCAR CCM3
787 and Its Sensitivity to Convection Parameterization, *J. of Clim.*, 2851-2866, 2006.

788 Cooper, O. R., Eckhardt, S., Crawford, J. H., Brown, C. C., Cohen, R. C., Bertram, T. H.,
789 Wooldridge, P., Perring, A., Brune, W.H., Ren, X., Brunner, D., and Baughcum, S. L.:
790 Summertime buildup and decay of lightning NO_x and aged thunderstorm outflow above
791 North America, *J. Geophys.Res.*, 114, D01101, doi:10.1029/2008JD010293, 2009.

792 Dickerson, R. R., Huffman, G. J., Luke, W. T., Nunnermacker, L. J., Pickering, K. E. , Leslie,
793 A., Lindsey, C., Slinn, W., Kelly, T., Daum, P., Delany, A., Grennberg, J., Zimmerman,
794 P., Boatman, J., Ray, J., and Stedman, D.: Thunderstorms: An important mechanism in
795 the transport of air pollutants, *Science*, 235, 460 – 465, 1987.

796 Dong, L. and Colucci, S. J. : The Role of Deformation and Potential Vorticity in Southern
797 Hemisphere Blocking Onsets, *J. Atmos. Sci.*, 62, 4043-4056, 2005.

798 Drummond, J. W., D. H. Ehhalt, and A. Volz, Measurements of nitric oxide between 0 – 12
799 km altitude and 67° N-60° S latitude obtained during STRATOZ III, *J. Geophys. Res.*,
800 93, 15,831 – 15,849, 1988.

801 Emmons, L. K., Hauglustaine, D. A., Muller, J.-F., Carroll, M. A., Brasseur, G. P., Brunner, D.,
802 Staehelin, J., Thouret, V., and Marenco, A.: Data composites of tropospheric ozone and
803 its precursors from aircraft measurements, *J. Geophys. Res.*, 105, 20,497 – 20,538, 2000.

804 Evett, R. R., Mohrle C. R., Hall B. L., Brownb T. J. and Stephens S. L.: The effect of monsoonal
805 atmospheric moisture on lightning fire ignitions in southwestern North America,
806 *Agricultural and forest meteorology*, 148, 1478–1487, 2008.

807 Fadnavis, S., Semeniuk, K., Pozzoli, L., Schultz, M. G., Ghude, S. D., Das, S. and Kakatkar, R.:
808 Transport of aerosols into the UTLS and their impact on the Asian monsoon region as
809 seen in a global model simulation, *Atmos. Chem. Phys.*, 13, 8771–8786, 2013,
810 doi:10.5194/acp-13-8771-2013.Fadnavis S, Schultz M. G., Semeniuk K., Mahajan A. S.,
811 Pozzoli L., Sonbawne S., Ghude S. D., Kiefer M., and Eckert E., Trends in Peroxyacetyl
812 Nitrate (PAN) in the Upper Troposphere and Lower Stratosphere over Southern Asia
813 during the summer monsoon season: Regional Impacts, *Atmos. Chem. Phys.*, 14, 12725–
814 12743, doi:10.5194/acp-14-12725-2014, 2014.

815 Fiore, A. M., Horowitz, L. W., Purves, D. W., Levy II, H., Evans, M. J., Wang, Y., Li, Q., and
816 Yantosca, R. M.: Evaluating the contribution of changes in isoprene emissions to surface
817 ozone trends over the eastern United States, *J. Geophys. Res.*, 110, D12303,
818 doi:10.1029/2004JD005485, 2005.

819 Fischer E. V., Jacob D. J., Yantosca R. M., Sulprizio M. P., Millet D. B., Mao J., Paulot F.,
820 Singh H. B., Roiger A., Ries L., Talbot R.W., Dzepina K., and Pandey Deolal S.,
821 Atmospheric peroxyacetyl nitrate (PAN): a global budget and source attribution, *Atmos.*
822 *Chem. Phys.*, 14, 2679–2698, doi:10.5194/acp-14-2679-2014, 2014.

823 Fischer, H. and Oelhaf, H.: Remote sensing of vertical profiles of atmospheric trace constituents
824 with MIPAS limb-emission spectrometers, *Appl. Optics*, 35, 2787–2796, 1996.

825 Fischer, H., Birk, M., Blom, C., Carli, B., Carlotti, M., von Clarmann, T., Delbouille, L., Dudhia,
826 A., Ehhalt, D., Endemann, M., Flaud, J. M., Gessner, R., Kleinert, A., Koopman, R.,
827 Langen, J., Lopez-Puertas, M., Mosner, P., Nett, H., Oelhaf, H., Perron, G., Remedios, J.,
828 Ridolfi, M., Stiller, G., and Zander, R.: MIPAS: an instrument for atmospheric and
829 climate research, *Atmos. Chem. Phys.*, 8, 2151–2188, 2008, doi:10.5194/acp-8-2151-
830 2008.

831 Fu, R., Hu, Y., Wright, J. S., Jiang, J. H., Dickinson, R. E., Chen, M., Filipiak, M., Read, W. G.,
832 Waters, J.W. and Wu, D. L.: Short circuit of water vapour and polluted air to the global
833 stratosphere by convective transport over the Tibetan Plateau, Proc Natl Acad Sci U S A.
834 Apr 11, 103(15), 5664-9, Epub Apr 3, 2006.

835 Galanter, M., H. Levy II, and G. R. Carmichael (2000), Impacts of biomass burning on
836 tropospheric CO, NO_x, and O₃, J. Geophys. Res., 105(D5), 6633–6653,
837 doi:10.1029/1999JD901113.

838 Ganzeveld, L., and Lelieveld, J.: Dry deposition parameterization in a chemistry general
839 circulation model and its influence on the distribution of reactive trace gases, J. Geophys.
840 Res.,100(D10), 20999–21012, doi:10.1029/95JD02266, 1995.

841 Garny, H., and Randel, W. J.: Dynamic variability of the Asian monsoon anticyclone observed in
842 potential vorticity and correlations with tracer distributions, J. Geophys. Res. Atmos.,
843 118, 13,421–13,433, doi:10.1002/2013JD020908, 2013.

844 Gettelman, A., Salby, M. L., and Sassi, F.: Distribution and influence of convection in the
845 tropical tropopause region, J. Geophys. Res., 107(D10), 4080,
846 doi:10.1029/2001JD001048, 2002.

847 Gettelman, A., Hoor, P., Pan, L. L., Randel, W. J., Hegglin, M. I., and Birner, T.: The
848 extratropical upper troposphere and lower stratosphere, Rev. Geophys., 49, RG3003,
849 doi:10.1029/2011RG000355, 2011.

850 Glatthor, N., Clarmann, T. von, Fischer, H., Funke, B., Grabowski, U., Höpfner, M., Kellmann,
851 S., Kiefer, M., Linden, A., Milz M., Steck, T., and Stiller, G.P.: Global peroxyacetyl
852 nitrate (PAN) retrieval in the upper troposphere from limb emission spectra of the
853 Michelson Interferometer for Passive Atmospheric Sounding (MIPAS), Atmos. Chem.
854 Phys., 7, 2775-2787, www.atmos-chem-phys.net/7/2775/2007/ doi:10.5194/acp-7-2775-
855 2007, 2007.

856 Grewe, V., Brunner, D., Dameris, M., Grenfell, J.L., Hein, R., Shindell, D. and Staehelin, J. :
857 Origin and Variability of Upper Tropospheric Nitrogen Oxides and Ozone at Northern
858 Mid-Latitudes. *Atmos. Environ.*, 35, 3421-3433, 2001.

859 Harris, R. C., et al., The Amazon boundary layer experiment (ABLE 2A) dry season 1985, *J.*
860 *Geophys. Res.*, 93, 1351-1360, 1988.

861 Harriss, R.C., S.C. Wofsy, D.S. Bartlett, M.C. Shipham, D.J. Jacob, J.M. Hoell, Jr., R.J.
862 Bendura, J.W. Drewry, R.J. McNeal, R.L. Navarro, R.N. Gidge, and V.E. Rabine, The
863 Arctic Boundary Layer Expedition (ABLE 3A): July-August 1988, *J. Geophys. Res.*, 97,
864 16,383-16,394, 1992.

865 Harriss, R.C., S.C. Wofsy, J.M. Hoell, Jr., R.J. Bendura, J.W. Drewry, R.J. McNeal, D. Pierce,
866 V.Rabine, and R.L. Snell, The Arctic Boundary Layer Expedition (ABLE-3B): July-
867 August 1990, *J. Geophys. Res.*, 99, 1635-1643, 1994.

868 Hassim, M. E. E., Lane, T. P., and May, P. T.: Ground-based observations of overshooting
869 convection during the Tropical Warm Pool-International Cloud Experiment, *J. Geophys.*
870 *Res. Atmos.*, 119, 880–905, doi:10.1002/2013JD020673, 2014.

871 Hoell, J. M., Jr., D. L. Albritton, G. L. Gregory, R. J. McNeal, S. M. Beck, R. J. Bendura, and J.
872 W. Drewry, Operational overview of NASA GTE/CITE 2 airborne
873 instrumentintercomparisons: Nitrogen dioxide, nitric acid, and peroxyacetyl nitrate, *J.*
874 *Geophys. Res.*, 95, 10,047-10,054, 1990.

875 Hoell, J. M., Jr., D. L. Albritton, G. L. Gregory, R. L. McNeal, S. M. Beck, R. J. Bendura, and J,
876 W. Drewry, Operational overview of NASA GTE/CITE-2 airborne instrument
877 intercomparison: Nitrogen dioxide, nitric acid, and peroxyacetyl nitrate. *J. Geophys.*
878 *Res.*, 95, 10,047-10,054, 1990

879 Horowitz, L. W., Walters, S., Mauzerall, D. L., Emmons, L. K., Rasch, P. J., Granier, C., Tie, X.,
880 Lamarque, J., Schultz, M. G., Tyndall, G. S., Orlando, J. J. and Brasseur, G. P.: A global
881 simulation of tropospheric ozone and related tracers, Description and evaluation of
882 MOZART, version 2, *J. Geophys. Res.*, 108(D24), 2003.

883 Hudman, R. C., Jacob, D. J., Cooper, O. R., Evans, M. J., Heald, C. L., Park, R. J., Fehsenfeld,
884 F., Flocke, F., Holloway, J., Hübler, G., Kita, K., Koike, M., Kondo, Y., Neuman, A.,
885 Nowak, J., Oltmans, S., Parrish, D., Roberts, J. M., and Ryerson, T.: Ozone production in
886 transpacific Asian pollution plumes and implications for ozone air quality in California, *J.*
887 *Geophys. Res.*, 109, D23S10, doi:10.1029/2004jd004974, 2004.

888 Hudman, R. C., Jacob, D. J., Turquety, S., Leibensperger, E. M., Murray, L. T., Wu, S.,
889 Gilliland, A. B., Avery, M., Bertram, T. H., Brune, W., Cohen, R. C., Dibb, J. E., Flocke,
890 F. M., Fried, A., Holloway, J., Neuman, J. A., Orville, R., Perring, A., Ren, X., Ryerson,
891 T. B., Sachse, G. W., Singh, H. B., Swanson, A., and Wooldridge, P. J.: Surface and
892 lightning sources of nitrogen oxides over the United States: magnitudes, chemical
893 evolution, and outflow, *J. Geophys. Res.*, 112, D12S05, doi:10.1029/2006JD007912,
894 2007.

895 Keim, C., Liu, G. Y., Blom, C.E., Fischer, H., Gulde, T., Höpfner, M., Piesch, C., Ravegnani,
896 F., Roiger, A., Schlager, H., and Sitnikov, N.: Vertical profile of peroxyacetyl nitrate (PAN)
897 from MIPAS-STR measurements over Brazil in February 2005 and its contribution to
898 tropical UT NO_y partitioning, *Atmos. Chem. Phys.*, 8, 4891-4902, doi:10.5194/acp-8-4891-
899 2008, 2008.

900 Khaykin S., Pommereau, J.-P., Korshunov, L., Yushkov, V., Nielsen, J., Larsen, N.,
901 Christensen, T., Garnier, A., Lukyanov, A., and Williams, E.: Hydration of the lower
902 stratosphere by ice crystal geysers over land convective systems, *Atmos. Chem. Phys.*, 9,
903 2275–2287, 2009.

904 Kulkarni J.R., Maheshkumar, R.S., Morwal, S.B., Padma kumari, B., Konwar, M., Deshpande,
905 C.G., Joshi, R.R., Bhalwankar, R.V., Pandithurai, G., Safai, P.D., Narkhedkar, S.G.,

906 Dani, K.K., Nath, A., Nair, Sathy, Sapre, V.V., Puranik, P.V., Kandalgaonkar, S.S.,
907 Mujumdar, V.R., Khaladkar, R.M., Vijaykumar, R., Prabha, T.V., Goswami, B.N., The
908 Cloud Aerosol Interaction and Precipitation Enhancement Experiment (CAIPEEX):
909 overview and preliminary results (2012), *Curr. Sci.*, Vol.102, 2012, 413-425.

910 Labrador, L. J., Kuhlmann, R. von, and Lawrence, M. G.: The effects of lightning-produced
911 NO_x and its vertical distribution on atmospheric chemistry: sensitivity simulations with
912 MATCH-MPIC, *Atmos. Chem. Phys.*, 5, 1815–1834, 2005.

913 Lamsal, L. N., Martin, R. V., Padmanabhan, A., van Donkelaar, A., Zhang, Q., Sioris, C. E.,
914 Chance, K., Kurosu, T. P., and Newchurch, M. J.: Application of satellite observations
915 for timely updates to global anthropogenic NO_x emission inventories, *Geophys. Res.*
916 *Lett.*, 38,L05810, doi:10.1029/2010GL046476, 2011.

917 Li, Q., Jiang, J. H., Wu, D. L., Read, W. G., Livesey, N. J., Waters, J. W., Zhang, Y., Wang, B.,
918 Filipiak, M. J., Davis, C. P., Turquety, S., Wu, S., Park R. J., Yantosca R. M., and Jacob
919 D. J.: Convective outflow of South Asian pollution: A global CTM simulation compared
920 with EOS MLS observations, *Geophys. Res. Lett.*, 32, L14826,
921 doi:10.1029/2005GL022762, 2005.

922 Liang, Q., Rodriguez, J. M., Douglass, A. R., Crawford, J. H., Olson, J. R., Apel, E., Bian, H.,
923 Blake, D. R., Brune, W., Chin, M., Colarco, P. R., da Silva, A., Diskin, G. S.,
924 Duncan, B. N., Huey, L. G., Knapp, D. J., Montzka, D. D., Nielsen, J. E., Pawson, S.,
925 Riemer, D. D., Weinheimer, A. J., and Wisthaler, A.: Reactive nitrogen, ozone and ozone
926 production in the Arctic troposphere and the impact of stratosphere-troposphere
927 exchange, *Atmos. Chem. Phys.*, 11, 13181-13199, doi:10.5194/acp-11-13181-2011,
928 2011.

929 Liu, C., and Zipser E. J.: Global distribution of convection penetrating the tropical tropopause, *J.*
930 *Geophys. Res.*, 110, D23104, 2005.

931 Martin, R. V., Sauvage, B., Folkins, I., Sioris, C. E., Boone, C., Bernath, P., and Ziemke, J.:
932 Space-based constraints on the production of nitric oxide by lightning, *J. Geophys. Res.*,
933 112, D09309, doi:10.1029/2006JD007831, 2007.

934 Miyazaki, K., Eskes, H. J., and Sudo, K.: Global NO_x emission estimates derived from an
935 assimilation of OMI tropospheric NO₂ columns, *Atmos. Chem. Phys.*, 12, 2263–2288,
936 doi:10.5194/acp-12-2263-2012, 2012.

937 Murray, L. T., Jacob, D. J., Logan, J. A., Hudman, R. C., and Koshak, W. J.: Optimized regional
938 and interannual variability of lightning in a global chemical transport model constrained
939 by LIS/OTD satellite data, *J. Geophys. Res.*, 117, D20307, doi:10.1029/2012JD017934,
940 2012.

941 O'Sullivan D. W., • Heikes B. G Lee., M., Chang W., Gregory G. L., • Blake D. R., and Sachs
942 G. W., Distribution of hydrogen peroxide and methylhydroperoxide over the Pacific and
943 South Atlantic Oceans, *J. Geophys. Res.*, 104, D5, 5635-5646, 1999.

944 Pan L. L., A. Kunz, C. R. Homeyer , L. A. Munchak, D. E. Kinnison , and S. Tilmes,
945 Commentary on using equivalent latitude in the upper troposphere and lower
946 stratosphere, *Atmos. Chem. Phys.*, 12, 9187–9199, doi:10.5194/acp-12-9187-2012 ,
947 2012,

948 Park M., Randel W. J., Gettleman, A., Massie, S. T., and Jiang, J. H.: Transport above the
949 Asian summer monsoon anticyclone inferred from Aura Microwave Limb Sounder
950 tracers, *J. Geophys. Res.*, 112, D16309, doi:10.1029/2006JD008294, 2007.

951 Park, M., Randel, W. J., Emmons, L. K., and Livesey, N. J.: Transport pathways of carbon
952 monoxide in the Asian summer monsoon diagnosed from Model of Ozone and Related
953 Tracers (MOZART), *J. Geophys. Res.*, 114, D08303, doi:10.1029/2008JD010621, 2009.

954 Park, M., Randel, W. J., Kinnison, D. E., Garcia, R. R., and Choi, W.: Seasonal variation of
955 methane, water vapour, and nitrogen oxides near the tropopause: Satellite observations
956 and model simulations, *J. Geophys. Res.*, doi:10.1029/2003JD003706, 109, D03302,
957 2004.

958 Penki, R. K. and Kamra, A. K.: Lightning distribution with respect to the monsoon trough
959 position during the Indian summer monsoon season, *J. Geophys. Res.*, 118, 4780–4787,
960 doi:10.1002/jgrd.50382, 2013.

961 Pozzoli, L., Bey, I., Rast, J. S., Schultz, M. G., Stier, P., and Feichter, J.: Trace gas and aerosol
962 interactions in the fully coupled model of aerosol-chemistry-climate ECHAM5-
963 HAMMOZ: 1. Model description and insights from the spring 2001 TRACE-P
964 experiment, *J. Geophys. Res.*, 113, D07308, doi:10.1029/2007JD009007, 2008a.

965 Pozzoli, L., Bey, I., Rast, J. S., Schultz, M. G., Stier, P., and Feichter, J.: Trace gas and aerosol
966 interactions in the fully coupled model of aerosol-chemistry-climate ECHAM5-
967 HAMMOZ: 2. Impact of heterogeneous chemistry on the global aerosol distributions, *J.*
968 *Geophys. Res.*, 113, D07309, doi:10.1029/2007JD009008, 2008b.

969 Pozzoli, L., Janssens-Maenhout, G., Diehl, T., Bey, I., Schultz, M. G., Feichter, J., Vignati, E.,
970 and Dentener, F.: Re-analysis of tropospheric sulfate aerosol and ozone for the period
971 1980–2005 using the aerosol-chemistry-climate model ECHAM5-HAMMOZ, *Atmos.*
972 *Chem. Phys.*, 11, 9563-9594, doi:10.5194/acp-11-9563-2011, 2011.

973 Prabha T.V., Khain A., Maheshkumar R.S., Pandithurai G., Kulkarni J.R., Goswami B.N.
974 (2011), Microphysics of Premonsoon and Monsoon Clouds as Seen from In Situ
975 Measurements during the Cloud Aerosol Interaction and Precipitation Enhancement
976 Experiment (CAIPEEX), *J. Atm. Sc.*, Vol.68 , 2011, DOI: 10.1175/2011JAS3707.1,
977 1882-1901

978 Price, C. and Asfur, M.: Inferred long term trends in lightning activity over Africa, *Earth Planets*
979 *Space*, 58, 1197–1201, 2006.

980 Ranalkar, M. R and Chaudhari, H. S.: Seasonal variation of lightning activity over the Indian
981 subcontinent. *Meteorology and Atmospheric Physics*. 104, 125–134, 2009.

982 Randel, W. J. and Park, M.: Deep convective influence on the Asian summer monsoon
983 anticyclone and associated tracer variability observed with Atmospheric Infrared Sounder
984 (AIRS), *J. Geophys. Res.*, 111, D12314, doi:10.1029/2005JD006490, 2006.

985 Randel, W. J., Moyer, E., Park, M., Jensen, E., Bernath, P., Walker, K., and Boone C.: Global
986 variations of HDO and HDO/H₂O ratios in the upper troposphere and lower stratosphere
987 derived from ACE-FTS satellite measurements, *J. Geophys. Res.*, 117, D06303,
988 doi:10.1029/2011JD016632, 2012.

989 Randel, W. J., Park, M., Emmons, L., Kinnison, D., Bernath, P., Walker, K. A., Boone, C. and
990 Pumphrey H.: Asian monsoon transport of pollution to the stratosphere, *Science*. Apr
991 30,328(5978),611-3. Epub Mar 25, 2010.

992 Rast, S., M.G. Schultz, I. Bey, T. van Noije and co-authors, Evaluation of the tropospheric
993 chemistry general circulation model ECHAM5–MOZ and its application to the analysis
994 of the chemical composition of the troposphere with an emphasis on the late RETRO
995 period 1990–2000 Technical rapport: 2014, Max Planck Institute of Meteorology, Earth
996 System Science, 74p. Real, E., Orlandi, E., Law, K. S., Fierli, F., Josset, D., Cairo, F.,
997 Schlager, H., Borrmann, S., Kunkel, D., Volk, C. M., McQuaid, J. B., Stewart, D. J., Lee,
998 J., Lewis, A. C., Hopkins, J. R., Ravegnani, F., Ulanovski A. and Lioussse C.: Cross-
999 hemispheric transport of central African biomass burning pollutants: implications for
1000 downwind ozone production, *Atmos. Chem. Phys.*, 10, 3027–3046, 2010.

1001 Ridley, B. A., Madronich, S., Chatfield, R. B., Walega, J. G., Shetter, R. E., Carroll, M. A.,
1002 and Montzka D. D: Measurements and model simulations of the photostationary state
1003 during the Mauna Loa Observatory Photochemistry Experiment: Implications for radical
1004 concentrations and ozone production and loss rates, *J. Geophys. Res.*, 97(D10), 10375–
1005 10388, doi:10.1029/91JD02287, 1992.

1006 Ridley, B.A., J.G. Walega, J.E. Dye, and F.E. Grahek, Distributions of NO, NO_x, NO_y, and O₃ to
1007 12 km altitude during the summer monsoon season over New Mexico, *J. Geophys. Res.*,
1008 99, 25,519-25,534, 1994.

1009 Roeckner, E., Bauml, G., Bonaventura, L., Brokopf, R., Esch, M., Giorgetta, M., Hagemann, S.,
1010 Kirchner, I., Kornblueh, L., Manzini, E., Rhodin, A., Schlese, U., Schulzweida, U., and
1011 Tompkins, A.: The atmospheric general circulation model ECHAM5: Part 1, Tech. Rep.
1012 349, Max Planck Institute for Meteorology, Hamburg, 2003.

1013 Sander, S. P. Fried, R. R., Barker, J. R., Golden, D. M., Kurylo, M. J., Wine, P. H., J. Abbatt P.
1014 D., Burkholder, J. B., Kolb, C. E., Moortgat, G. K., Huie, R. E., Orkin, V. L.: Chemical
1015 kinetics and photochemical data for use in atmospheric studies, evaluation number 14,
1016 JPL Publ. 02-25, Jet Propul. Lab., Calif. Inst. of Technol., Pasadena. (Available
1017 at http://jpldataeval.jpl.nasa.gov/pdf/JPL_02-25_rev02.pdf), 2003.

1018 Schmitz, J. T., Mullen S. L., 1996: Water Vapor Transport Associated with the Summertime
1019 North American Monsoon as Depicted by ECMWF Analyses. *J. Climate*, **9**, 1621–1634.,
1020 1996.

1021 Schultz, M., Backman, L., Balkanski, Y., Bjoerndalsaeter, S., Brand, R., Burrows, J., Dalsoeren,
1022 S., de Vasconcelos, M., Grodtmann, B., Hauglustaine, D., Heil, A., Hoelzemann, J.,
1023 Isaksen, I., Kaurola, J., Knorr, W., Ladstaetter-Weienmayer, A., Mota, B., Oom, D.,
1024 Pacyna, J., Panasiuk, D., Pereira, J., Pulles, T., Pyle, J., Rast, S., Richter, A., Savage, N.,
1025 Schnadt, C., Schulz, M., Spessa, A., Staehelin, J., Sundet, J., Szopa, S., Thonicke, K., van
1026 het Bolscher, M., van Noije, T., van Velthoven, P., Vik, A., and Wittrock, F.: REanalysis
1027 of the TROpospheric chemical composition over the past 40 years (RETRO). A long-
1028 term global modeling study of tropospheric chemistry. Final Report, Tech. rep., Max
1029 Planck Institute for Meteorology, Hamburg, Germany, 2007.

1030 Schultz, M. G., Heil, A., Hoelzemann, J. J., Spessa, A., Thonicke, K., Goldammer, J. G., Held,
1031 A. C., Pereira, J. M. C., and van het Bolscher, M.: Global wildland fire emissions from
1032 1960 to 2000, *Global Biogeochem. Cy.*, 22, GB2002, doi:10.1029/2007GB003031, 2008

1033 Schultz, M.G., T. Pulles, R. Brand, M. Van het Bolscher and S.T. Dalsøren, , A global data set of
1034 anthropogenic CO, NO_x, and NMVOC emissions for 1960-2000, in preparation and
1035 available at <http://eccad.sedoo.fr/>

1036 Schultz, M.G, A. Heil, J.J. Hoelzemann, A. Spessa, K. Thonicke, J. Goldammer, A.C. Held, J.M.
1037 Pereira, M. Van Het Bolscher, 2005: Global Wildland Fire Emissions from 1960 to 2000,
1038 doi:10.1029/2007GB003031 , *Global Biogeochemical Cycles* 22 (GB2002) : 17 PP

1039 Schumann, U. and Huntrieser, H.: The global lightning-induced nitrogen oxides source, *Atmos.*
1040 *Chem. Phys.*, 7, 3823–3907, 2007.

1041 Shepon, A., Gildor, H., Labrador, L. J., Butler, T., Ganzeveld, L. N., and Lawrence, M. G.:
1042 Global reactive nitrogen deposition from lightning NO_x, *J. Geophys. Res.*, 112, D06304,
1043 doi:10.1029/2006JD007458, 2007.

1044 Singh, H. B., Viezee, W., Chen, Y., Thakur, A. N., Kondo, Y. and Talbot, R. W.,Gregory, G. L.,
1045 Sachse, G. W., Blake, D. R., Bradshaw, J. D., Wang, Y., and Jacob D. J.: Latitudinal
1046 distribution of reactive nitrogen in the free troposphere over the Pacific Ocean in late
1047 winter/early spring, *J. Geophys. Res.*, 103(D21), 28237–28246, doi:10.1029/98JD01891,
1048 1998.

1049 Singh, H. B.,Reactive nitrogen in the troposphere, *Environ. Sci. Technol.*, 21(4), 320–327, 1987

1050 Singh, H.B., Salas, L.J. and Viezee, W.: Global distribution of peroxyacetyl nitrate, *Nature*, Jun
1051 5-11;321(6070):588-91, 1986.

1052 Singh, H. B., Brune W. H., Crawford J. H., Jacob D. J., and Russell P. B.: Overview of the
1053 summer 2004 Intercontinental Chemical Transport Experiment – North America
1054 (INTEX-A), *J. Geophys. Res.*, 111, 2006, D24S01, doi:10.1029/2006JD007905.

1055 Stier, P., Feichter, J., Kinne, S., Kloster, S., Vignati, E., Wilson, J., Ganzeveld, T., Tegen, I.,
1056 Werner, M., Balkanski, Y., Schulz, M., Boucher, O., Minikin, A., and Petzold, A.: The
1057 aerosol climate model ECHAM5-HAM, *Atmos. Chem. Phys.* 5, 1125– 1165,
1058 doi:10.5194/acp-5-1125-2005, 2005.

1059 Talbot, R. W., Dibb, J. E., Scheuer, E. M., Bradshaw, J. D., Sandholm, S. T., Singh, H. B.,
1060 Blake, D. R., Blake, N. J., Atlas, E., and Flocke, F.: Tropospheric reactive odd nitrogen
1061 over the South Pacific in austral springtime, *J. Geophys. Res.*, 105, 6681–6694,
1062 doi:10.1029/1999JD901114, 2000.

1063 Talukdar, R. K., Burkholder, J. B., Schmoltner, A., Roberts, J. M., Wilson, R. R. and
1064 Ravishankara, A. R.: Investigation of loss processes for peroxyacetyl nitrate in the
1065 atmosphere: UV photolysis and reaction with OH, *J. Geophys. Res.*, 100, 14163–14173,
1066 1995.

1067 Tang, J. H., Chan, L. Y., Chang, C. C., Liu, S., and Li, Y. S.: Characteristics and sources of non-
1068 methane hydrocarbons in background atmospheres of eastern, southwestern, and southern
1069 China, *J. Geophys. Res.*, 114, D03304, doi:10.1029/2008JD010333, 2009.

1070 Tereszchuk K. A., Moore D. P., Harrison J. J., Boone C. D., Park M., Remedios J. J., Randel W.
1071 J., and Bernath P. F., Observations of peroxyacetyl nitrate (PAN) in the upper
1072 troposphere by the Atmospheric Chemistry Experiment Fourier Transform Spectrometer
1073 (ACE-FTS), *Atmos. Chem. Phys.*, 13, 5601–5613, doi:10.5194/acp-13-5601-2013, 2013.

1074 Tie, X.X., Zhang, R., Brasseur, G., Emmons, L. and Lei, W.: Effects of lightning on reactive
1075 nitrogen and nitrogen reservoir species in the troposphere. *Journal of Geophysical*
1076 *Research-Atmospheres*, **106**, 3167-3178, DOI: 10.1029/2000JD900565, 2001.

- 1077 Uppala S. M., Kållberg P. W., Simmons A. J.*, Andrae U., Costa Bechtold V. Da, Fiorino
1078 M., Gibson J. K., Haseler J., Hernandez A., Kelly G. A., Li X., Onogi K., Saarinen
1079 S., Sokka N., Allan R. P., Andersson E., Arpe K., Balmaseda M. A., Beljaars A. C.
1080 M., Berg L. Van De, Bidlot J., Bormann N., Caires S., Chevallier F., Dethof A.,
1081 Dragosavac M., Fisher M., Fuentes M., Hagemann S., Hólm E., Hoskins B. J.,
1082 Isaksen L., Janssen P. A. E. M., Jenne R., McNally A. P., Mahfouf J.-F., Morcrette J.-
1083 J., Rayner N. A., Saunders R. W., Simon P., Sterl A., Trenberth K. E., Untch A.,
1084 Vasiljevic D., Viterbo P. and Woollen J.,
1085 The ERA-40 re-analysis, *Q. J. R. Meteorol. Soc.*, 131(612), 2961–3012, doi:10.1256/qj.04.176,
1086 2005.
- 1087 Vaughan G. and Timmis C.: Transport of near-tropopause air into the lower midlatitude
1088 stratosphere, *Q. J. R. Meteorol. SOC.*, 124, pp. 1559-1578, 1998.
- 1089 Von Clarmann, T., Höpfner, M., Kellmann, S., Linden, A., Chauhan, S., Funke, B., Grabowski,
1090 U., Glatthor, N., Kiefer, M., Schieferdecker, T., Stiller, G. P., and Versick, S.: Retrieval of
1091 temperature, H₂O, O₃, HNO₃, CH₄, N₂O, ClONO₂ and ClO from MIPAS reduced
1092 resolution nominal mode limb emission measurements, *Atmos. Meas. Tech.*, 2, 159–175,
1093 doi:10.5194/amt-2- 2159-2009, 2009.
- 1094 Wiegele A., Glatthor N., Hopfner M., Grabowski U., Kellmann S., Linden A., Stiller G., and von
1095 Clarmann T.: Global distributions of C₂H₆, C₂H₂, HCN, and PAN retrieved from MIPAS
1096 reduced spectral resolution measurements, *Atmos. Meas. Tech.*, 5, 723–734,
1097 doi:10.5194/amt-5-723-2012, 2012,
- 1098 Xiong, X., Houweling, S., Wei, J., Maddy, E., Sun, F., and Barnett, C.: Methane plume over
1099 South Asia during the monsoon season: Satellite observation and model simulation,
1100 *Atmos. Chem. Phys.*, 9, 783– 794, 2009.
- 1101 Zhang, L, Jacob, D. J., Boersma, K. F., Jaffe, D. A., Olson, J. R., Bowman, K. W., Worden, J.
1102 R., Thompson, A. M., Avery, M. A., Cohen, R. C., Dibb, J. E., Flock, F. M., Fuelberg, H.
1103 E., L. Huey, G., McMillan, W.W., Singh, H. B., and Weinheimer, A. J.: Transpacific
1104 transport of ozone pollution and the effect of recent, Asian emission increases on air

1105 quality in North America: an integrated analysis using satellite, aircraft, ozonesonde, and
1106 surface observations, *Atmos. Chem. Phys.*, 8, 6117–6136, 2008.

1107 Zhao, C., Wang, Y., Choi, Y., and Zeng, T.: Summertime impact of convective transport and
1108 lightning NO_x production over North America: modeling dependence on meteorological
1109 simulations, *Atmos. Chem. Phys.*, 9, 4315–4327, 2009.

1110 Ziereis, H., H. Schlager, P. Schulte, P.F.J. van Velthoven, and F. Slemr, Distributions of NO,
1111 NO_x, and NO_y in the upper troposphere and lower stratosphere between 28°N and 61°N
1112 during POLINAT 2, *J. Geophys. Res.*, **105**, 3653, 2000.

1113

1114

1115 Table 1: Global aircraft measurements used for model evaluation.

Experiment	Date Frame	Species	Location
<u>POLINAT-2</u> (Falcon) Ziereis et al.2000	Sep 19-Oct 25, 1997	O ₃ , NO _x	Canary-Islands: LAT= 25°N, 35°N, LON=160°W, 170°W E-Atlantic: LAT= 35°N, 45°N, LON=150°W,160°W Europe: LAT= 45°N, 55°N, LON=5°E, 15°E Ireland: LAT=50°N, 60°N, LON= 165°W,175°W
<u>PEM-Tropics-A</u> (DC8) Talbot et al. (2000)	Aug 24-Oct 15, 1996	O ₃ , NO _x , HNO ₃ , PAN	Christmas-Island: LAN= 0°, 10°N, LON=20°W, 40°W Easter-Island: LAT=-40°N, 20°S, LON=60°W, 80°W Fiji: LAT= 0°,10°S. LON= 170°E, 10°W Iawaii: LAT= 10°N, 30°N, LON= 10°W., 30°W Tahiti: LAT= 20°S, 0°, LON= 20°W, 50°W
<u>PEM-Tropics-A</u> (P3) O'Sullivan et al, 1999	Aug 15-Sep 26, 1996	O ₃ , HNO ₃	Christmas-Island: LAT= 0°, 10°N, LON= 20°W, 40°W Easter-Island: LAT= 40°S, 20°S, LON= 60°W, 80°W Hawaii: LAT= 10°N, 30°N, LON= 10°W, 30°W Tahiti: LAT= 20°S, 0°, LON= 20°W, 50°W
<u>ABLE-3B</u> (Electra) Harriss et al.,1994	Jul 6-Aug 15, 1990	O ₃ , NO _x , HNO ₃ , PAN	Labrador: LAT= 50°N, 55°N, LON= 120°W, 135°W Ontario: LAT= 45°N, 60°N, LON= 90°W, 100°W US-E-Coast: LAT= 35°N, 45°N, LON= 100°W, 110°W.
<u>CITE-3</u> (Electra) Hoell et al 1993	Aug 22-Sep 29, 1989	O ₃ , NO _x	Natal: LAT= 15°S.,5°N, LON= 145°W, 155°W Wallops: LAT= 30°N, 40°N, LON= 100°W, 110°W
<u>ELCHEM</u> (Sabreliner) Ridley et al.,1999	Jul 27-Aug 22, 1989	O ₃ , NO _x	New-Mexico: LAT=30°N, 35°N , LON= 70°W, 75°W
<u>ABLE-3A</u> (Electra) Harriss et al.,1992	Jul 7-Aug 17, 1988	O ₃ , NO _x ,PAN	Alaska: LAT= 55°N, 75°N, LON= 10°W, 25°W
<u>ABLE-2A</u> (Electra) Harris et al., 1988	Jul 12-Aug 13, 1985	O ₃	E-Brazil: LAT= 10°S, 0°, LON= 120°W, 135°W W-Brazil: LAT= 5°S, 0°, LON= 110°W, 120°W
<u>STRATTOZ-3</u> (Caravelle 116) Drummond et al., 1988	Jun 4-26, 1984	O ₃	Brazil: LAT= 20°S, 0°, LON= 135°W, 155°W Canary-Islands: LAT= 20N, 35N, LON= 160°W, 155°W E-Tropical-N-Atlantic: LAT= 0°, 20°N, LON=150W.,165W. England: LAT= 45°N, 60°N, LON= 10°E, 5°W Goose-Bay: LAT= 45°N, 60°N, LON= 110°W, 125°W Greenland: LAT= 60N, 70N, LON= 110W, 150W Iceland: LAT= 60N, 70N, LON= 150W, 155W NW-South-America: LAT=-5°N, 10°N, LON= 95°W, 115°W Puerto-Rico: LAT= 10°N, 25°N, LON= 110°W, 120°W S-South-America: LAT= 65S,45S, LON= 95W, 120W SE-South-America: LAT= 45°S, 20°S. LON= 115°W, 140°W. SW-South-America: LAT=-45°S,25°S, LON= 105°W, 112°W Spain: LAT= 35°N, 45°N, LON= 15W, 0° W-Africa: LAT= 0., 15°N, LON= 15°W, 0°. W-South-America: LAT= 25°S, 5°S. LON=

			95°W,110°W Western-N-Atlantic: LAT= 25°N, 45°N, LON= 110°W,120°W
<u>CITE-2</u> (Electra) Hoell et al., 1990	Aug 11-Sep 5, 1986	O ₃ , NO _x , HNO ₃ , PAN	Calif: LAT= 35°N, 45°N, LON= 55°W, 70°W Pacific: LAT= 30°N, 45°N, LON= 45°W, 55°W
INTEX-A,Singh et al. (2006)	Jul–Aug 2004	O ₃ ,PAN,NO _x	Eastern North America: LAT= 29°N, 51°N, Lon: 44°W-120°W
CAIPEEX (Prabha et al., 2011)	Sep 2010 –Oct 2010	O ₃ , NO _x	Lat=12°N,22°N, Lon=74°E, 78°E

1116

1117

1118

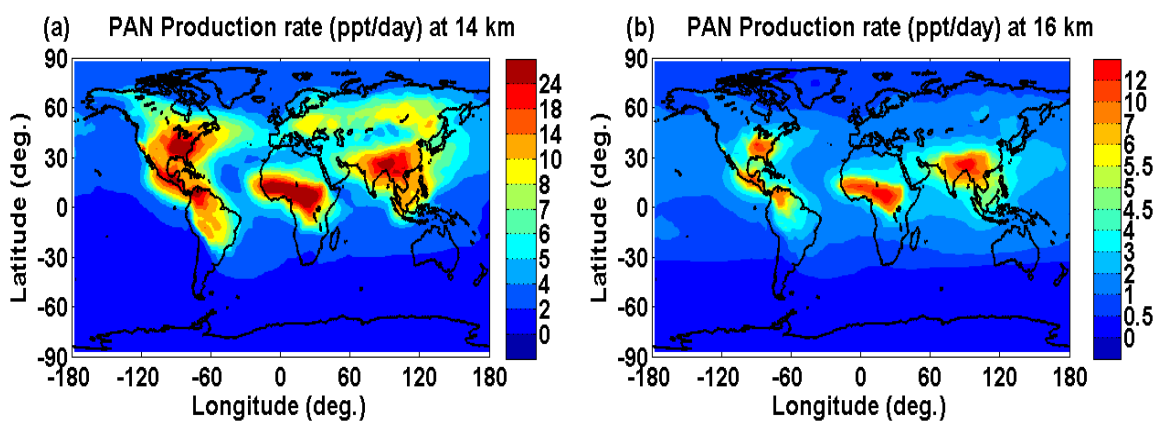
1119

1120

1121

1122

1123



1124 Figure 1. PAN production rates at (a) 14 km and (b) 16 km. Key regions of biomass burning and

1125 anthropogenic emissions of pollutants are evident and correspond to maxima in PAN production.

1126 Weaker dispersed background formation is evident as well.

1127

1128

1129

1130

1131

1132

1133

1134

1135

1136

1137

1138

1139

1140

1141

1142

1143

1144

1145

1146

1147

1148

1149

1150

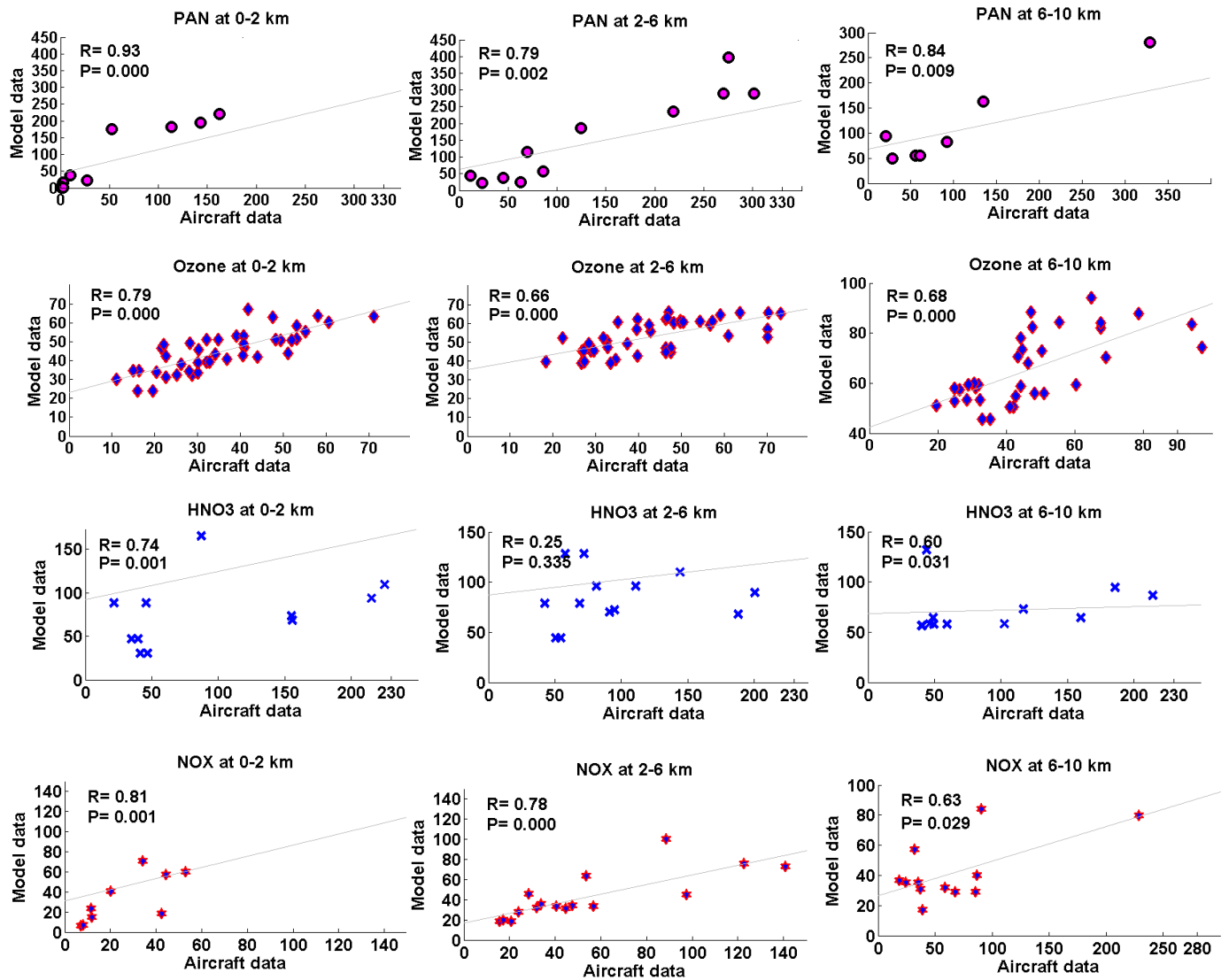


Figure 2. Scatter plot between model simulation (averaged for 1995-2004) and aircraft observations of PAN (ppt), ozone (ppb), HNO₃ (ppt), NO_x (ppt) (averaged for the monsoon season (June-September)). The model simulations and aircraft observations are averaged for altitude ranges over the coherent regions. The Pearson's correlation coefficient (R) and corresponding p-value is given in each subplot.

1151

1152

1153

1154

1155

1156

1157

1158

1159

1160

1161

1162

1163

1164

1165

1166

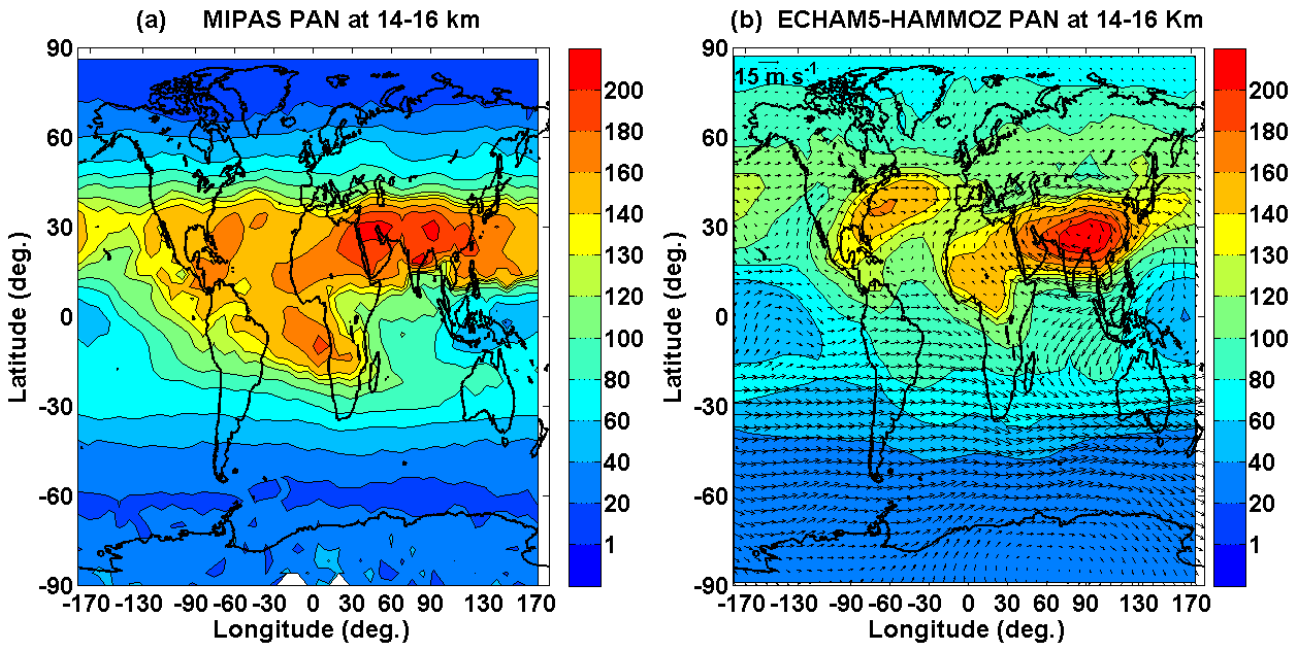
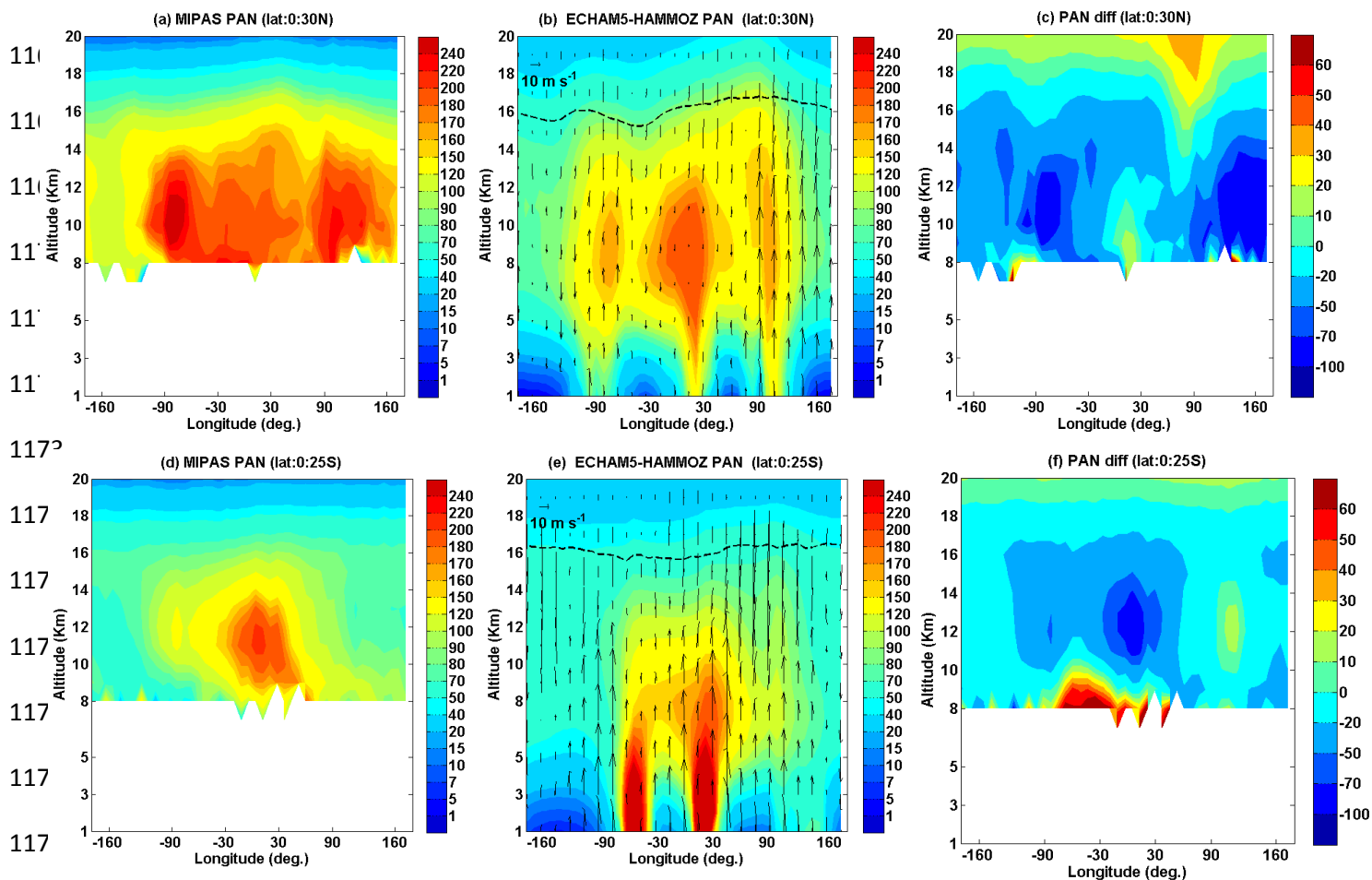


Figure 3. Distribution of seasonal mean PAN concentration (ppt) averaged for 14 -16 km (a) observed by MIPAS-E (climatology for the period 2002-2011) (b) ECHAM5-HAMMOZ CTRL simulations. Wind vectors at 16 km are indicated by black arrows in figures (b)



1180
 1181 Figure 4. Longitude-altitude cross section of PAN (ppt) averaged for monsoon season and 10°N
 1182 -30°N ; (a) MIPAS-E climatology (b) ECHAM5-HAMMOZ CTRL simulations. (c) difference in
 1183 PAN (ppt) (MIPAS - ECHAM5-HAMMOZ). PAN (ppt) averaged for monsoon season and $0-$
 1184 25°S (d) MIPAS-E climatology (e) ECHAM5-HAMMOZ CTRL simulations (f) difference in
 1185 PAN (ppt) (MIPAS - ECHAM5-HAMMOZ). ECHAM5-HAMMOZ simulations are smoothed
 1186 with averaging kernel of MIPAS-E. Wind vectors are indicated by black arrows in figures (b)
 1187 and (e). The vertical velocity field has been scaled by 300. The black line in (b) and (e) indicates
 1188 the tropopause.

1189

1190

1191

1192
 1193
 1194
 1195
 1196
 1197
 1198
 1199
 1200
 1201
 1202
 1203
 1204
 1205
 1206
 1207
 1208
 1209
 1210
 1211
 1212
 1213
 1214
 1215
 1216

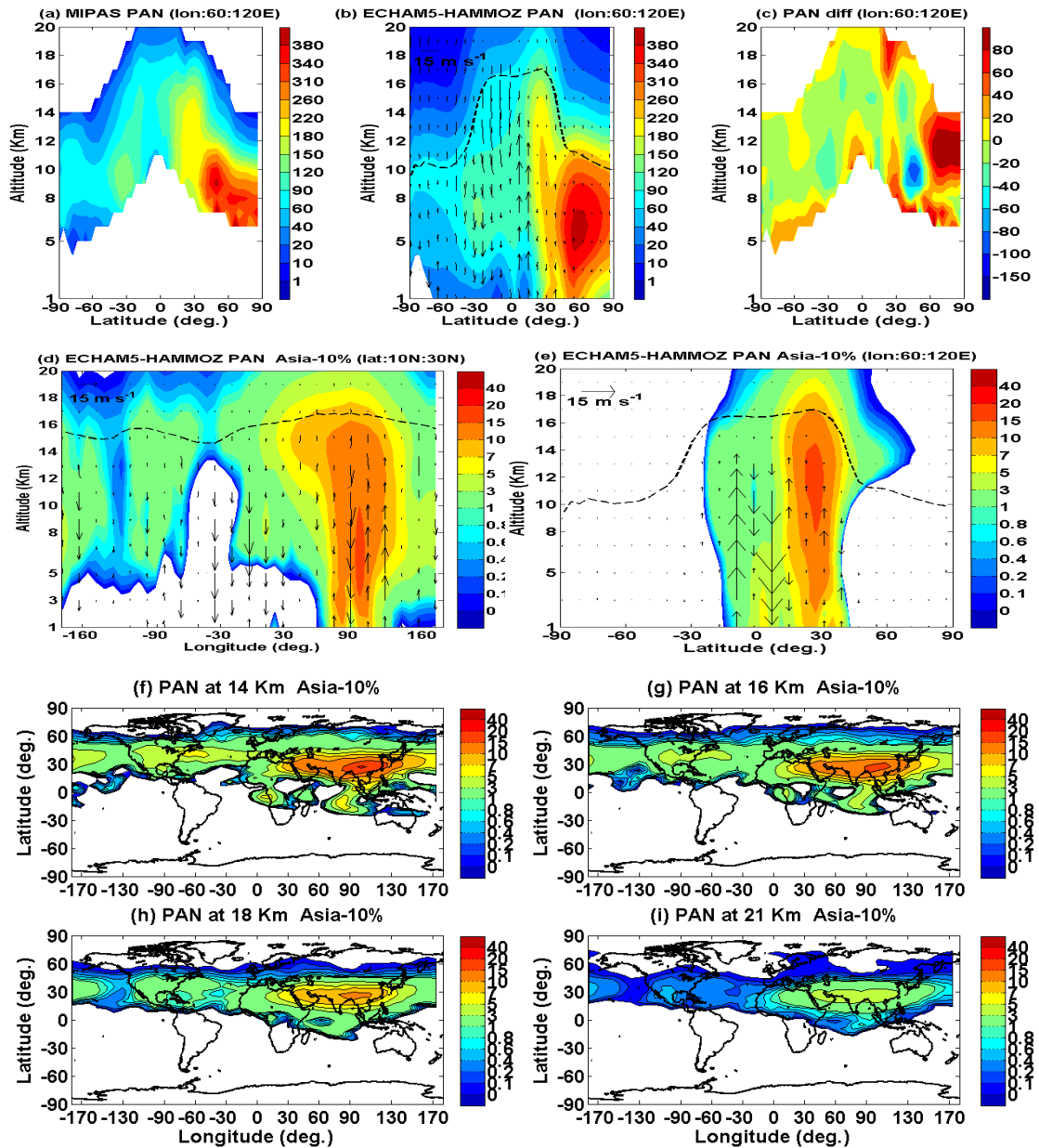
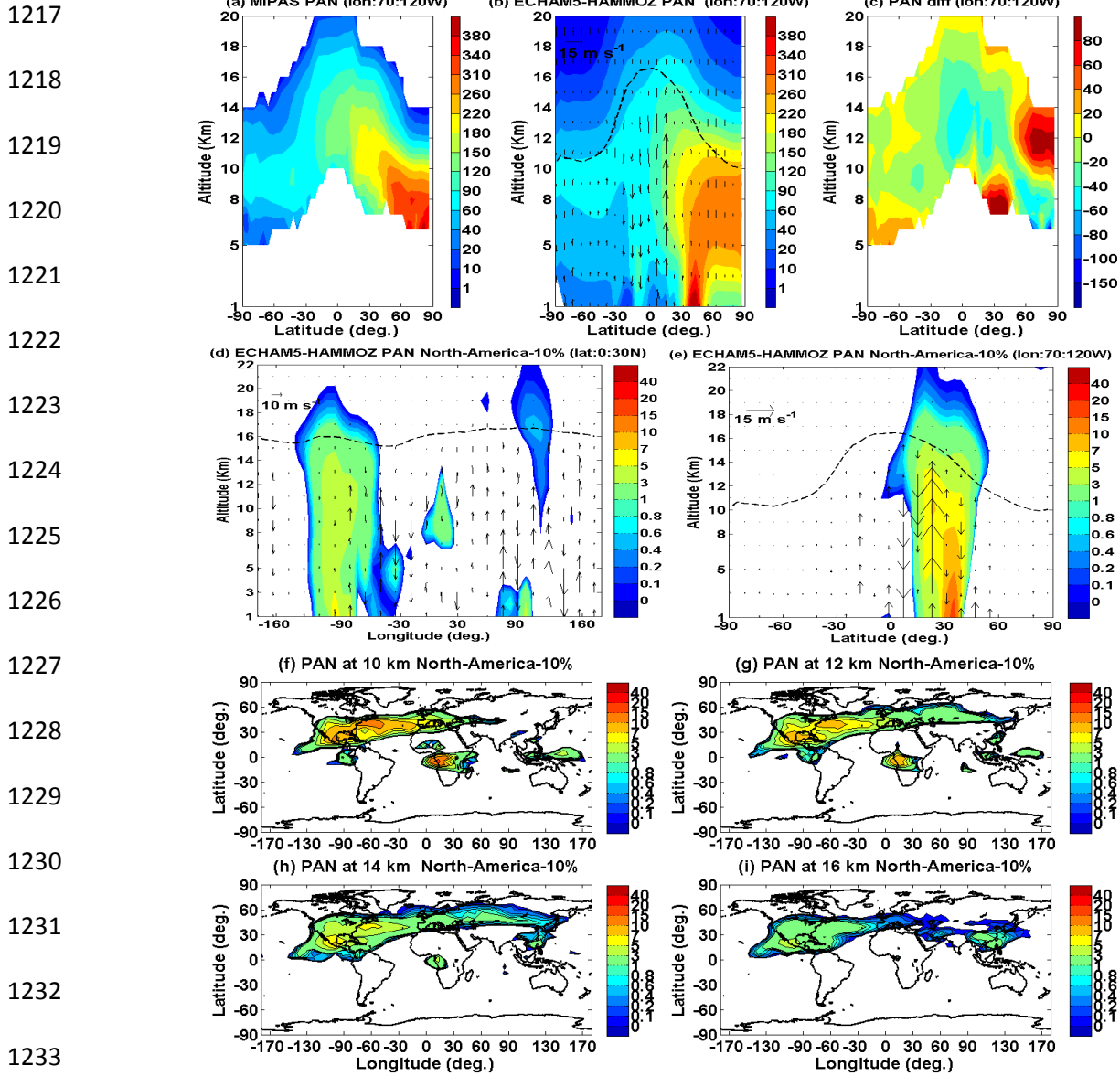
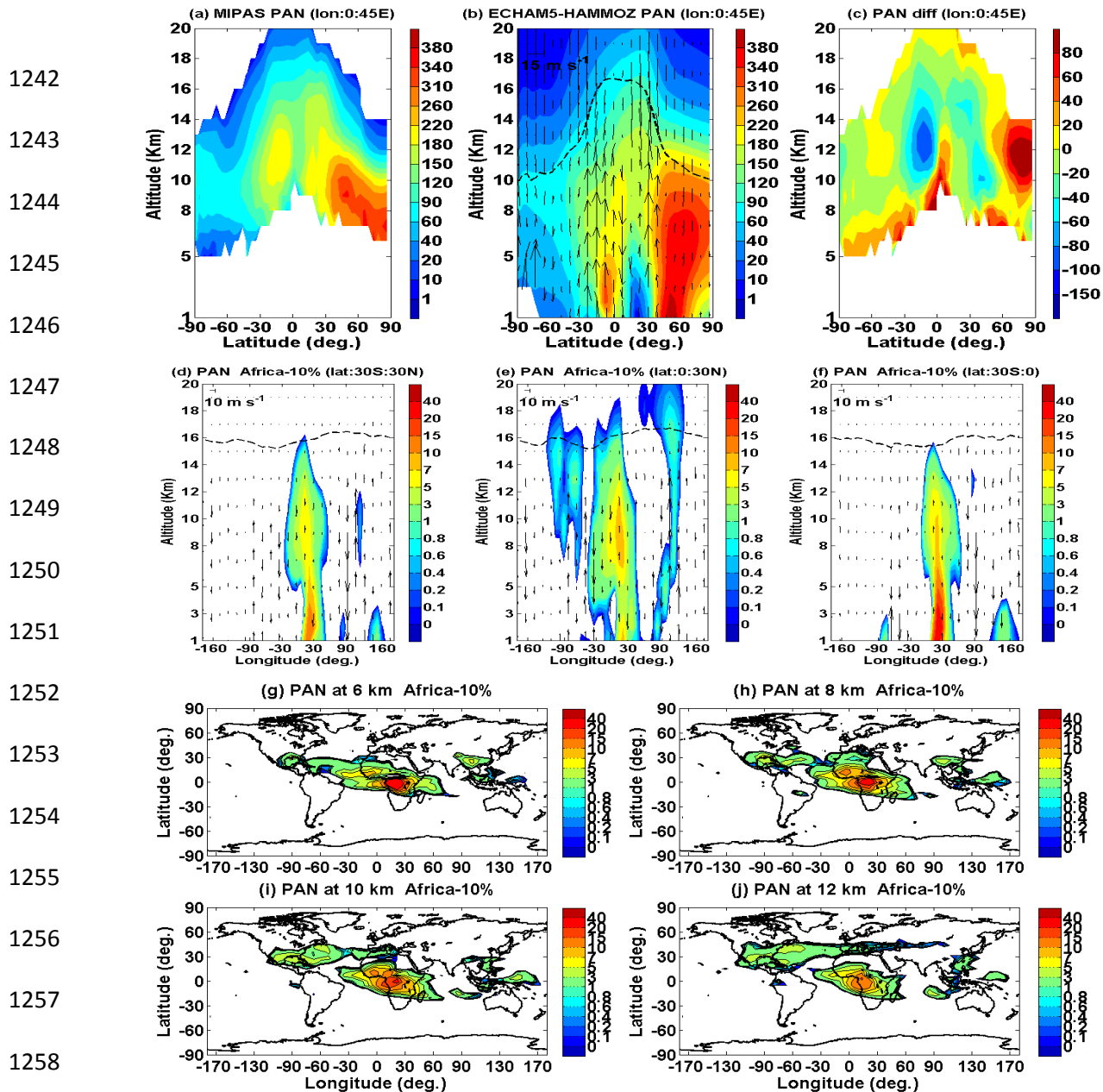


Figure 5. Latitude-altitude cross section of PAN (ppt) (a) MIPAS-E climatology, averaged for monsoon season and for 60-120° E, (b) PAN from ECHAM5-HAMMOZ CTRL simulations, averaged for monsoon season and 60-120° E, (c) difference in PAN (ppt) (MIPAS-ECHAM5-HAMMOZ), (d) longitude-altitude section averaged over 0 -30° N obtained from reference-Asia-10% simulations (e) same as (d) but latitude-altitude section averaged over 60-120°E, (f) – (i) latitude-longitude sections of reference – Asia-10% simulations at 14km, 16 km, 18 km , 21 km respectively. Wind vectors are indicated by black arrows. The vertical velocity field has been scaled by 300.



1234 Figure 6. Latitude-altitude cross section of PAN (ppt) (a) MIPAS-E climatology, averaged for
 1235 monsoon season and for 70-120⁰ W, (b) PAN from ECHAM5-HAMMOZ CTRL simulations,
 1236 averaged for monsoon season and 70-120⁰ E, (c) difference in PAN (ppt) (MIPAS-ECHAM5-
 1237 HAMMOZ), (d) longitude-altitude section averaged over 0 -30⁰ N obtained from reference-
 1238 North-America-10% simulations (e) same as (d) but latitude-altitude section averaged over
 1239 120⁰W-70⁰W, (f) –(i) latitude-longitude sections of reference – North-America-10% simulations
 1240 at 10km, 12 km 14km, 16 km respectively. Wind vectors are indicated by black arrows. The
 1241 vertical velocity field has been scaled by 300.



1259 Figure 7. Latitude-altitude cross section of PAN (ppt) (a) MIPAS-E climatology, averaged for
 1260 monsoon season and for 0-45° E, (b) PAN from ECHAM5-HAMMOZ CTRL simulations,
 1261 averaged for monsoon season and 0-45° E, (c) difference in PAN (ppt) (MIPAS-ECHAM5-
 1262 HAMMOZ), (d) longitude-altitude section averaged over 30°S - 30°N obtained from reference-
 1263 Africa-10% simulations (e) same as d but averaged over 0-30°N, (f) same as d but averaged over
 1264 0-30°S. Wind vectors are indicated by black arrows. The vertical velocity field has been scaled
 1265 by 300, Longitude – latitude section of PAN obtained from reference- Africa-10% simulations
 1266 at (g) 6 km, (h) 8 km, (i) 10 km, (j) 12km.

1267

1268

1269

1270

1271

1272

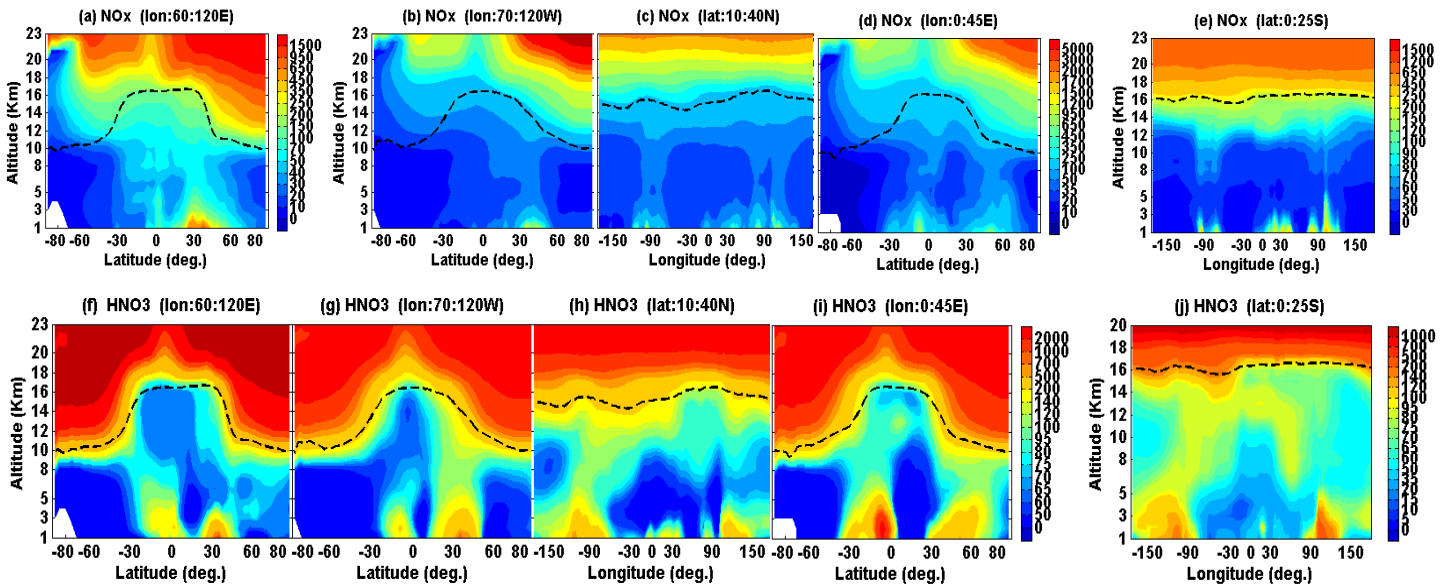
1273

1274

1275

1276

1277



1278

1279

1280

1281

1282

1283

1284

1285

1286

1287

1288

1289

1290

1291

Figure 8. Panel (a) Latitude-altitude cross section of seasonal mean ECHAM5-HAMMOZ NO_x (ppt) averaged for (a) 60° E-120° E, (b) 70° W-120° W, (c) longitude-altitude cross section averaged over 10° N-40° N, (d) latitude-altitude cross section averaged over 0-45° E and (e) longitude-altitude cross section averaged over 0-25° S, (f)-(i) same as (a)-(e) but for HNO₃.

1292

1293

1294

1295

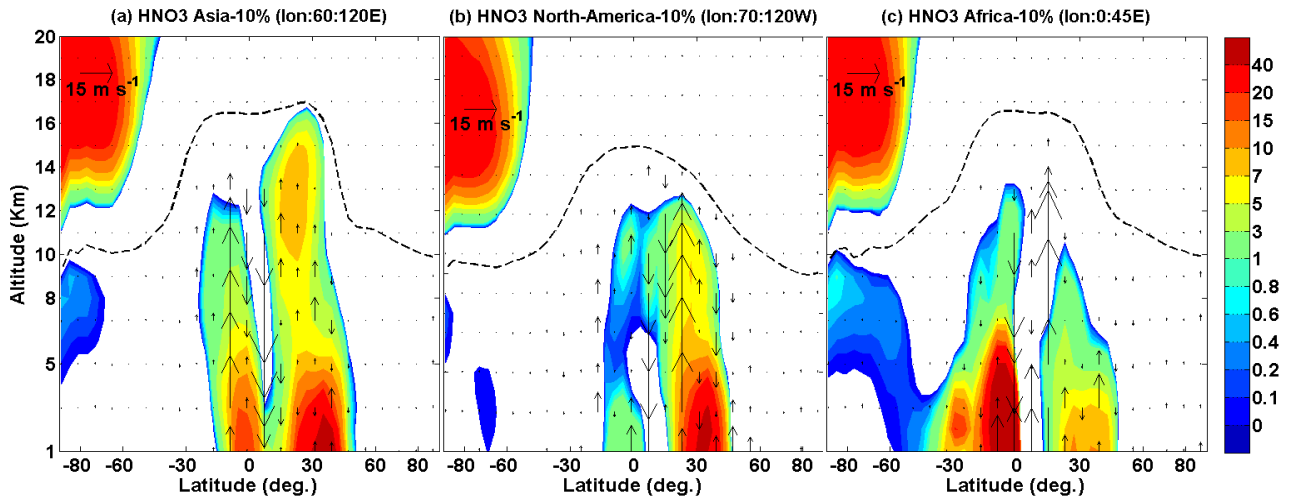
1296

1297

1298

1299

1300



1301

1302

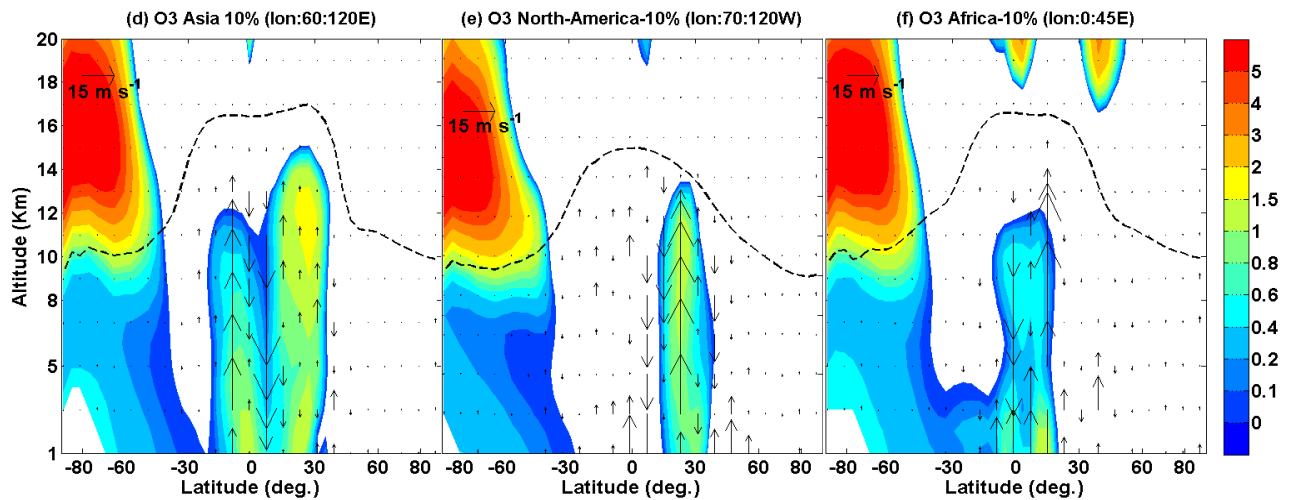
1303

1304

1305

1306

1307



1308

1309

1310

1311

1312

1313

1314

1315

1316

Figure 9. Latitude-altitude variation of (a) HNO₃ (Reference – Asia-10%) , averaged over 60⁰-120⁰E (b) HNO₃ (difference of Reference – North-America-10%) , averaged over 70⁰-120⁰W (c) HNO₃ (Reference – Africa-10%), averaged over 0-45⁰ E (d) O₃ (difference of Reference – Asia-10%) averaged over 60-120E (e) O₃ (Reference – North-America-10%) over North America averaged over 70⁰ -120⁰ W (f) O₃ (Reference – Africa-10%) over Africa averaged over 0-45(Reference – Africa-10%) . HNO₃ is expressed in ppt and ozone in ppb.

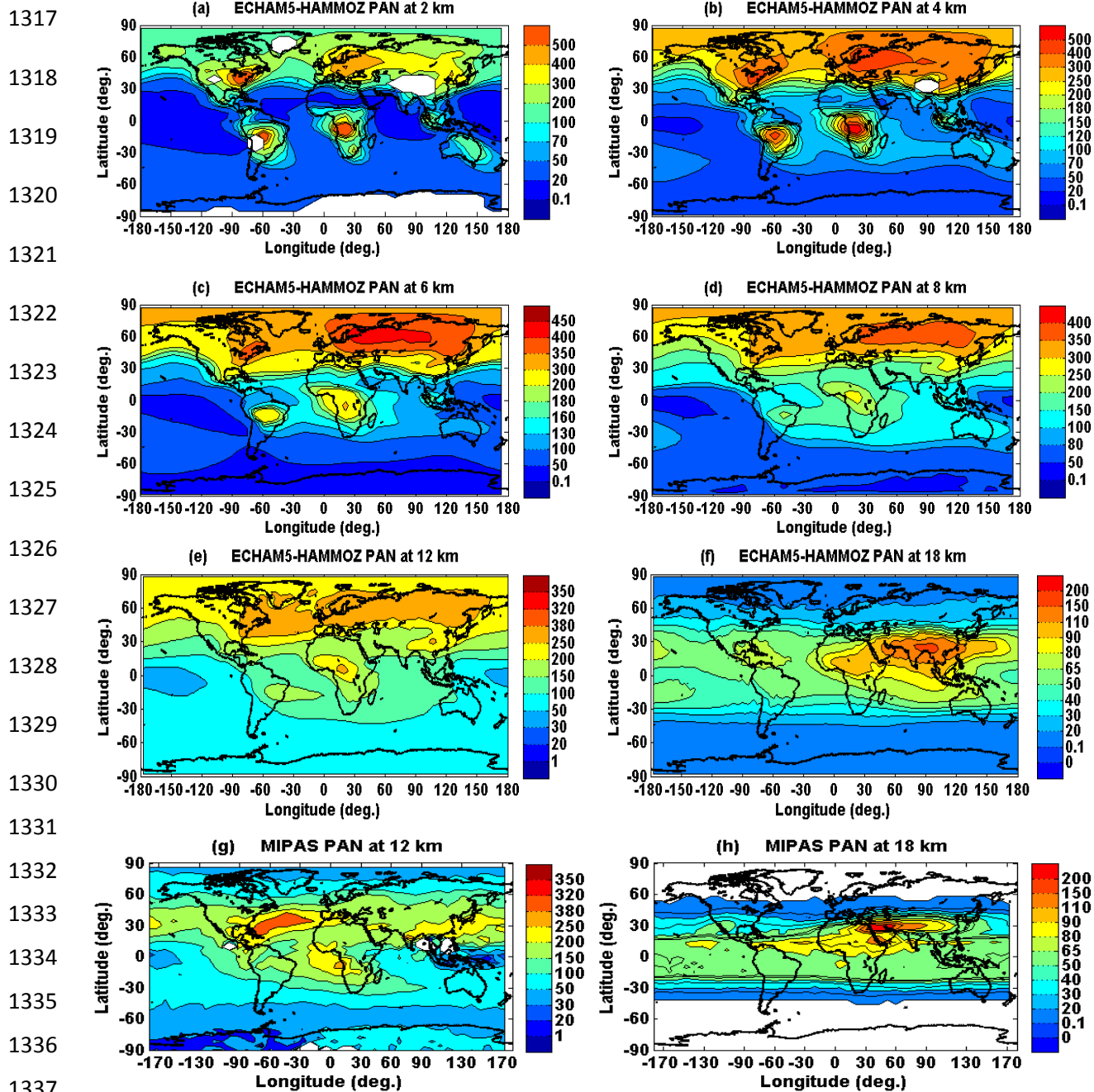
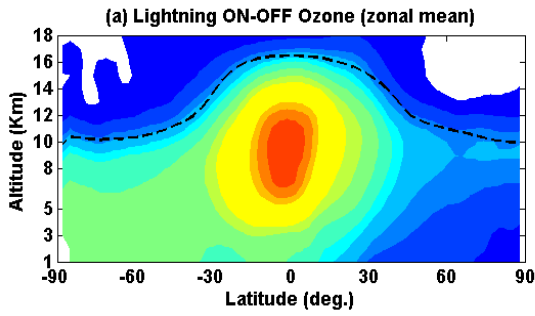
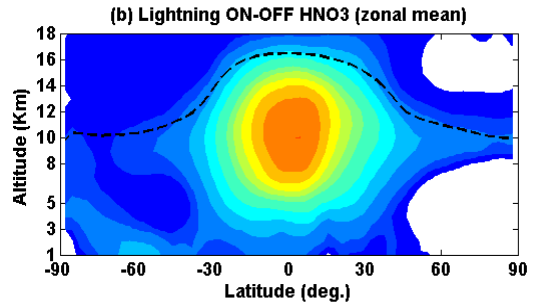


Figure 10. Latitude-longitude cross section of PAN (ppt) averaged for monsoon season (a) ECHAM5-HAMMOZ simulations at 2 km (b) 4 km (c) 6 km (d) 8 km (e) 12 km (f) 18 km. MIPAS-E climatology at (g) 12 km (h) 18 km.

1342



1343

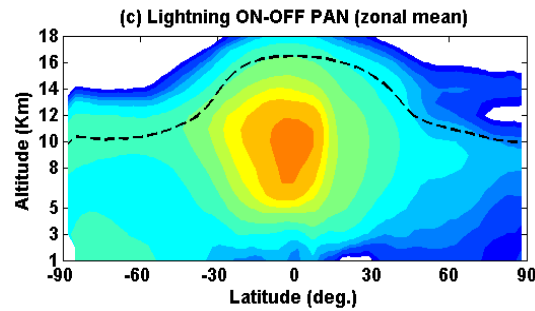


1344

1345

1346

1347

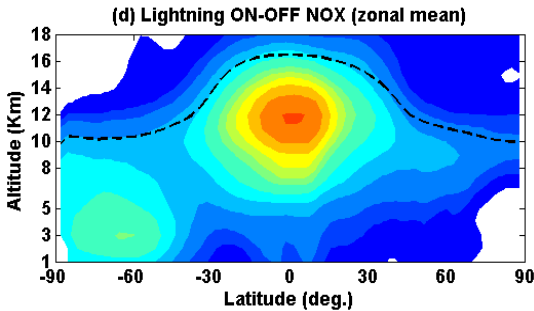


1348

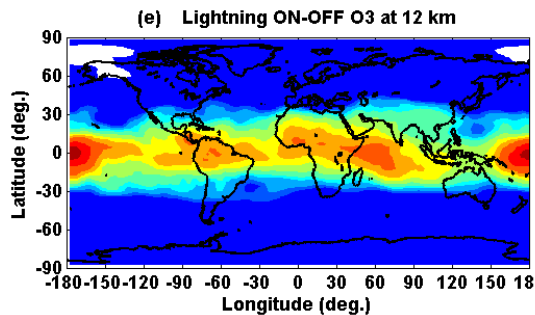
1349

1350

1351



1352

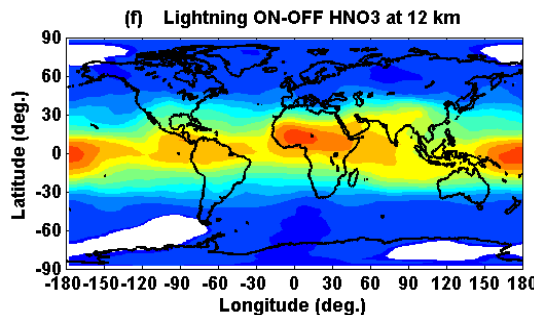


1353

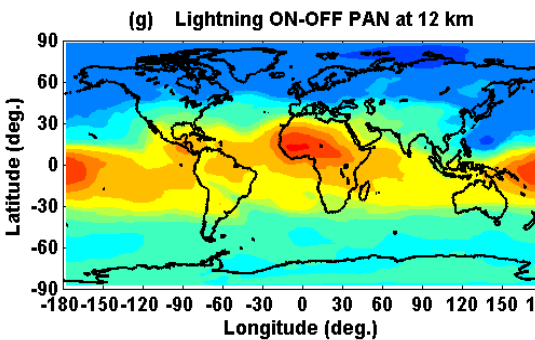
1354

1355

1356



1357

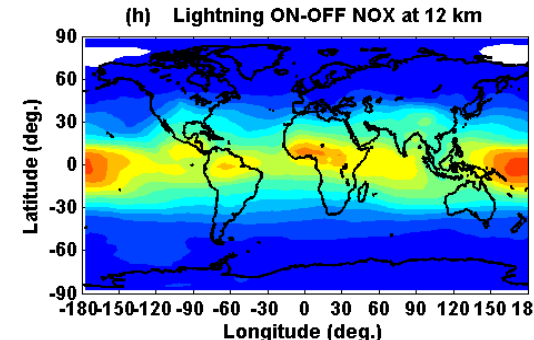


1358

1359

1360

1361



1362

1363

1364

1365

Figure 11. Zonal averaged seasonal mean changes (percentage) produced from lightning in (a) ozone (b) HNO₃ (c) PAN (d) NO_x, distribution of seasonal mean changes (percentage) produced from lightning in (e) ozone (f) HNO₃ (g) PAN (h) NO_x at 12 km.